Failure criteria for porous dome rocks and lavas: a study of Mt. Unzen, Japan

Rebecca Coats[1], Jackie E. Kendrick[1], Paul A. Wallace[1], Takahiro Miwa[2], Adrian J. Hornby[1,3], James D. Ashworth[1], Takeshi Matsushima[4], Yan Lavallée[1]

5 [1]Department of Earth, Ocean and Ecological Sciences, The University of Liverpool, Liverpool, L69 3GP, UK

[2]National Research Institute for Earth Science and Disaster Prevention, Ibaraki, 305-0006, Japan

[3]Now at Department of Earth and Environmental Sciences, Ludwig-Maximilians-Universität München, Munich, 80333, Germany

[4]Institute of Seismology and Volcanology, Kyushu University, Nagasaki, 855 0843, Japan

10 *Correspondence to*: Rebecca Coats (r.coats@liverpool.ac.uk)

Abstract

The strength and deformation mode (brittle vs ductile) of rocks is generally related to the porosity and pressure conditions, with occasional considerations of strain rate. At high temperature, molten rocks abide to Maxwell's viscoelasticity and their deformation mode (brittle vs ductile) is generally defined by strain rate or reciprocally, by comparing the relaxation
15 timescale of the material (for a given condition) to the observation timescale – a dimensionless ratio known as the Deborah (*De*) number. Volcanic materials are extremely heterogeneous, with variable concentrations of crystals, glass/ melt and vesicles (of different sizes), and a complete description of the conditions leading to flow or rupture as a function of temperature, stress and strain rate (or timescale of observation) eludes us. Here, we examined the conditions which lead to failure for variably vesicular (9-35%), crystal-rich (~ 75%), pristine and altered, dome rocks (at ambient temperature) and
20 lavas (at 900 °C) from Mt. Unzen Volcano, Japan. We found that the strength of the dome rocks decreases with porosity and is commonly independent of strain rate; when comparing pristine and altered rocks, we found that alteration caused minor strengthening. The strength of the lavas (at 900 °C) also decreases with porosity. Importantly, the results demonstrate that these dome rocks are weaker at ambient temperatures than when heated and deformed at 900 °C (for a given strain rate resulting in brittle behaviour). Thermal stressing (by heating and cooling a rock up to 900 °C at a rate of 4 °C min^{-1}, before
25 testing its strength at ambient temperature) was found not to affect the strength of rocks.

In the magmatic state (900 °C), the rheology of the dome lavas is strongly strain rate dependent. Under low strain rate conditions ($\leq 10^{-4}$ s^{-1}) the lavas behaved ductilely (i.e., the material sustained substantial, pervasive deformation) and displayed a non–Newtonian, shear thinning behaviour. In this regime, the apparent viscosities of the dome lavas were found to be independent of vesicularity, likely due to efficient pore collapse during shear. At high strain rates ($\geq 10^{-4}$ s^{-1}) the lavas
30 displayed an increasingly brittle response (i.e., deformation resulted in failure along localised faults); we observed an increase in strength and a decrease in strain–to–failure as a function of strain rate. To constrain the conditions leading to failure of the lavas, we analysed and compared the critical Deborah number at failure (*De$_c$*, the ratio between the relaxation time and the experimental observation time) of these lavas to that of pure melt (De$_{melt}$=10^{-3}-10^{-2}; Webb & Dingwell, 1990). We found that the presence of crystals decreases *De$_c$* to 2.11×10^{-4}. The vesicularity (φ), which dictates the strength of lavas,
35 further controls *De$_c$* following $-5.1\times10^{-4}\varphi+2.11\times10^{-4}$. We discuss the implications of these findings for the case of magma ascent and lava dome structural stability.

1 Introduction

1.1 Lava dome eruptions

Magma ascends to the Earth's surface and erupts through a wide spectrum of eruptive style (e.g. Siebert et al., 2015), which
contributes to the construction of different volcanic edifices (e.g. de Silva and Lindsay, 2015). Amongst this activity, lava
domes form when viscous magma accumulates and creates mounds of rocks and lava above the vent (Fink and Anderson,
2000). These dome–building events make up approximately 6% of volcanic eruptions worldwide (Calder et al. 2015) and
their characteristics are governed by the rheology of the erupted magmas (Gonnermann and Manga, 2007; Lavallée et al.,
2007). The emplacement of lava domes may be endogenous or exogenous, whether growing through inflation from within,
or through the piling up of discrete extrusive bodies (Hale and Wadge, 2008). In some extreme cases the latter can manifest
as lava spines, extrude in a near–solid state (Angelo Heilprin, 1903; Stasiuk and Jaupart, 1997; Young et al., 1998; Tanguy,
2004; Scott et al., 2008; Vallance et al., 2008; Kendrick et al., 2012; Cashman and Sparks, 2013). Dome eruptions can
produce a range of primary hazards, from ash fall to large–scale pyroclastic density currents, generated by gravitational
collapse (e.g. Sparks and Young, 2002). They also have the potential to generate secondary hazards such as lahars (e.g.
Nevado del Ruiz, Colombia; Pierson et al. 1990); edifice failure induced by magma intrusions (Voight and Elsworth, 1997;
Reid et al., 2010), and lava dome collapse, as the mass cools or redistributes (e.g. Elsworth and Voight, 1996). In seismically
active areas, strong tectonic earthquakes can both initiate activity and promote structural instability (e.g. Mayu–yama, Japan;
Siebert et al. 1987), even in long–dormant systems (e.g. Merapi, Indonesia; Surono et al. 2012). Thus, the eruption,
emplacement and stability of lava domes reflects the mechanical properties of the materials they consist of. It is therefore
essential to the continued monitoring effort of lava domes that the modelling and evaluation of their state be based on a
description of the mechanical and rheological properties of the materials for the development of improved forecasting tools.

1.2 Lava dome rheology

The rheology of silicate melts has been explored extensively (e.g. Dingwell and Webb, 1989, 1990; Webb and Dingwell,
1990; Webb and Knoche, 1996; Fluegel, 2007; Giordano et al., 2008; Cordonnier et al., 2012b). Dingwell and Webb (1989)
demonstrated that silicate liquids are viscoelastic bodies, that abide to the glass transition– a temperature–time space that
defines their structural relaxation according to the theory of viscoelasticity of Maxwell (1867). Maxwell's work established
that the structural relaxation time–scale τ equals the ratio between the melt viscosity η_m (in Pa.s) and its elastic modulus at
infinite frequency G_∞ (in Pa) according to:

$$\tau = \eta_m / G_\infty, \tag{1}$$

Dingwell and Webb (1989) compiled information for different silicate liquids and showed that G_∞ is essentially invariant
and approximately $10^{10\pm0.5}$ Pa in the temperature range of interest for magmatic systems. Thus, the relaxation time–scale of
silicate melts can simply be related to their viscosity at a given temperature. Extensive experimental efforts in the
community have resulted in the creation of a complete, non–Arrhenian model for silicate melt viscosity, as a function of
composition and temperature (Giordano et al., 2008). The concept of viscoelasticity and relaxation timescale can therefore
be applied to a range of volcanic processes.

Viscoelasticity dictates the behaviour of a magma. A rheological description of viscoelastic materials may be cast via the
non–dimensional Deborah number, De (e.g., Reiner 1964), which is defined by a ratio between Maxwell's relaxation time–
scale, τ (Eq. 1) and the time–scale of observation, t_{obs}:

$$De = \frac{\tau}{t_{obs}}, \qquad\qquad\qquad\qquad\qquad\qquad\qquad\qquad\qquad (2)$$

75   This relationship states that under observation timescales longer than the relaxation timescale (for a given melt viscosity), a melt may flow like a liquid; but at short observation timescales, a melt may behave as a solid (like a glass). In such a kinetic framework, increasing the temperature reduces the viscosity and therefore the time required for structural relaxation. As the relaxation time–scale is inversely proportional to the structural relaxation rate, it can thus be said that the structural relaxation rate defines the transition between the liquid and solid states (commonly referred to as the glass transition, T_g).

80   Dingwell and Webb (1990) demonstrated that at $De < 10^{-3}$, a silicate melt can be described as a Newtonian fluid. However, when silicate melts are deformed at higher rates where the observation time–scale is short, $10^{-3} < De < 10^{-2}$, the melt structure accumulates damage which results in an apparent non–Newtonian behaviour. At $De > 10^{-2}$, silicate melts undergo the glass transition and ruptures (Dingwell and Webb, 1990; Wadsworth et al., 2017); this is known as the critical Deborah number, De_c – a criteria met in several eruptive scenarios, including fragmentation and explosive eruptions (e.g. Dingwell, 85   1996).

During transport and eruption, magmas crystallise and volatiles are exsolved (e.g. Cashman, 1992; Martel and Schmidt, 2003), resulting in magmatic suspensions, undergoing significant rheological changes (e.g. Lejeune and Richet, 1995; Barmin et al., 2002). In particular, dome–building eruptions have been observed to produce variably vesicular (generally ≲ 40%) and crystalline (e.g. 0–100%) lavas (Castro et al., 2005; Mueller et al., 2005, 2011a; Lavallée et al., 2007; Pallister et 90   al., 2008; Cordonnier et al., 2009; Calder et al., 2015; Heap et al., 2016a). The addition of crystals to a melt increases the effective viscosity (Lejeune and Richet, 1995). At moderate crystal fraction (below ~ 25%) this can be approximated by the Einstein–Roscoe equation (Einstein, 1911; Roscoe, 1952), and variations thereof (see Mader et al., 2013 and references therein). When particle concentrations reach a critical fraction that promotes interaction (typically ≤ 0.25, depending on crystal morphology (Mader et al., 2013)), the suspension becomes non–Newtonian (Deubelbeiss et al., 2011). Experiments 95   on dome lavas have shown that the apparent viscosity of these suspensions decreases with strain rate (Lavallée et al., 2007; Avard and Whittington, 2012) - a shear thinning effect influenced by crystal alignment and interaction (Vona et al., 2011); crystal plasticity (Kendrick et al. 2017), and fracture processes (Lavallée et al., 2008; Kendrick et al., 2013b). The addition of a gas phase to a magma adds further complexity (Lejeune et al., 1999), serving to increase or decrease viscosity depending upon the volume fraction of bubbles, the initial viscosity of the melt, and the amount of deformation they are 100   subjected to (e.g. Manga et al., 1998; Llewellin and Manga, 2005). Bubbles will affect the viscosity of the suspension depending on their capillary number, Ca, a dimensionless ratio of the deforming viscous stress over the restoring stress from surface tension. A more spherical bubble will generally have a low Ca, as restoring stresses dominate, and will behave as a barrier which fluid flow will have to deviate around resulting in an increased viscosity of the suspension. On the other hand, an elongate bubble generally has a high Ca, as deforming stresses dominate, and may act as free slip surface causing a 105   decrease in the suspension viscosity (e.g. Manga et al., 1998; Mader et al., 2013). Three–phase models, although less explored than two–phase flows, have been modelled by Truby et al. (2015) by combining two sets of two–phase equations. Despite the aforementioned rheological studies focused on the viscosity of magmatic suspensions, the conditions leading to failure of such magmatic suspensions have received less attention. Following the work of Lavallée et al. (2007), Gottsmann et al. (2009) showed that the presence of crystals may reduce the strain rate required to rupture magma (if one was to 110   consider the melt relaxation rate) to conditions where $De < 10^{-2}$ and Lavallée et al. (2008) showed that brittle processes may be active at conditions two orders of magnitude lower than such a purely brittle limit. Cordonnier et al. (2012a) explored the effect of crystallinity on magma rupture, showing that De indeed decreases with crystallinity. However, here we note that when determining the Deborah number for their experimental findings, the relaxation time–scale was calculated using the apparent viscosity of the suspension rather than the viscosity of the interstitial melt, which is the basis for the applicability of 115   viscoelasticity in this scenario (this will be discussed further in section 5.2). Important questions remain as to the

contribution of vesicles on the rupture of magmas, as the strength of geomaterials in the brittle field is generally described in terms of porosity (e.g. Paterson and Wong, 2005, and references in section 1.3).

1.3 Lava dome mechanics

120 Various numerical models have been developed to evaluate the structural stability of lava domes and, with sufficient knowledge of a volcanic edifice and the properties of the materials it holds, collapse events can be modelled effectively (e.g. Elsworth and Voight, 1996). Although elegant and complex, these simulations tend to make non-trivial assumptions regarding vent geometry, dome morphology, and material properties (e.g. Ball et al., 2015). Volcanic domes are composed of materials with a vast spectrum of heterogeneities and degree of coherence (Mueller et al., 2011b; Lavallée et al., 2012, 2018) and although assigning fixed values for the material properties of dome rocks may be computationally beneficial,
125 accounting for the wide range of physical and mechanical properties of dome materials remain a great source of uncertainty. Mechanical testing can be carried out to resolve the behaviour of rocks (see Paterson and Wong, 2005 and references therein) and this has resulted in a recent surge in laboratory testing to advance the understanding of the tensile strength, compressive strength, frictional coefficient and flow behaviour of these heterogeneous dome rocks and magmas as a function of temperature and stresses or strain rates (Smith et al., 2007, 2011; Lavallée et al., 2007; Hess et al., 2008; Kendrick et al.,
130 2012, 2013a, 2013b; Kolzenburg et al., 2012; Heap et al., 2014a; Hornby et al., 2015; Lamb et al., 2017; Lamur et al., 2017 and more.)

The uniaxial compressive strength of volcanic rocks has been found to inversely correlate with porosity (Al-Harthi et al., 1999; Kendrick et al., 2013b; Heap et al., 2014a, 2014b, 2016b; Schaefer et al., 2015), and to positively correlate with strain rate (Schaefer et al., 2015). In volcanic rocks, porosity is made up of vesicles and micro–fractures, which contribute to the
135 mechanical behaviour and strength of the rock (Sammis and Ashby, 1986; Ashby and Sammis, 1990; Heap et al., 2014a; Bubeck et al., 2017; Collombet et al., 2017; Griffiths et al., 2017). Two models have gained traction to explain the strength of rocks. The pore–emanating crack model of Sammis and Ashby (1986), describes the case of a pore-only system where cracks nucleate from the pores and propagate in the direction parallel to the principal stress, when the applied stress overcomes the fracture toughness of a rock. As the applied stress increases, the micro–fractures propagate and coalesce,
140 leading to macroscopic failure. In contrast, the sliding wing–crack model of Ashby and Sammis (1990) considers only pre–existing micro–fractures inclined from the principal stress direction. The model describes that first, the frictional resistance of the crack must be overcome before wing cracks can form, then the fracture toughness must be overcome for them to propagate and interact. Heap et al., (2014a) experimentally demonstrated that a microstructural model that combines the two mechanisms must be considered when studying volcanic rocks, due to their microstructural complexity.

145 The problem of lava dome stability does not simply require knowledge of hot lavas or cold rocks; it further requires understanding of the effects of temperature (e.g. Harris et al., 2002); chemical alteration (e.g., Lopez & Williams 1993; Ball et al. 2015); pore pressure (Farquharson et al., 2016), thermal stressing (Heap et al., 2009, 2010, 2014a; Kendrick et al., 2013a; Schaefer et al., 2015) and mechanical stressing such as during seismic shaking (Cole et al., 1998; e.g. Voight, 2000; Calder et al., 2002) or magmatic intrusions (Walter et al., 2005) on the mechanical properties of the materials, many aspects
150 of which have been tested in the context of edifices. The cooling of crystalline lava bodies results in the generation of fractures (Fink and Anderson, 2000; Takarada et al., 2013) – leaving a highly fractured, blocky mass, the mechanical impact of which is difficult to quantify (Voight, 2000; Voight and Elsworth, 2000). Furthermore, thermal stressing cycles that could result from proximity of hot magma in a conduit, lava dome or edifice following a new eruptive episode, have been found to only weakly modify the strength of commonly micro-fractured volcanic rocks (Heap et al. 2009; Kendrick et al. 2013;
155 Schaefer et al. 2015,), unless they contain thermally liable minerals (Heap et al., 2012, 2013a, 2013b). Recent experiments

on porous basalt by Eggertsson et al. (*in review*) have shown that rocks that are essentially void of micro-cracks (likely due to slow cooling), are however susceptible to fracture damage by thermal stressing.

1.4 Mt. Unzen lava dome

The Unzendake volcanic complex is situated on the Shimabara peninsula in South–Western Japan (Fig. 1a). The volcanic
160 complex began to grow 0.5 Ma ago and now covers 20 km (E–W) by 25 km (N–S) (Takarada et al., 2013). Unzendake exhibits an intricate eruptive history of lava domes, flows and pyroclastic deposits (Nakada and Fujii, 1993) of predominantly dacitic composition (Nakada and Motomura, 1999).

On 17 November 1990, a phreatic eruption occurred at Mt. Unzen, which was accompanied by multiple earthquake swarms, after 198 years of quiescence (Matsushima and Takagi, 2000). This was followed shortly afterwards by a phreatomagmatic
165 eruption along with intense edifice swelling, and on 20 May 1991, the extrusion of a lava spine initiated the growth of the Heisei–Shinzan dome complex (Nakada and Fujii, 1993; Takarada et al., 2013). This introduced a 45-month long period of lava dome activity with growth being primarily exogenous in periods of high extrusion rate, and endogenous in times of low effusion rate (Nakada et al., 1995b, 1999a). The final stage of growth was marked by the extrusion of a spine between October 1994 and February 1995 (which can be seen this present day; Fig. 1c), characterised by pulsatory ascent and
170 seismicity (Umakoshi et al., 2008; Lamb et al., 2015), along fault zones defined by compactional shear (Ashworth et al.*, in prep*) and mineral reactions, crystal plasticity and comminution (Wallace et al., *submitted*). The end of the eruption was followed by cooling of the lava dome and thermal contraction that caused multiple joints (Takarada et al., 2013). Fumarole activity has continued to the present day, with temperatures decreasing from 300 °C in mid–2007 to 90 °C in 2011 (Takarada et al., 2013).

175 In total, 13 lava lobes were formed, and, at its maximum size, the lava dome was 1.2 km (E–W) by 0.8 km (N–S) wide. In particular lobe 11, which dominated the Eastern side of the complex (Nakada et al., 1995a, 1999b) has long been unstable, which has led to partial collapses that generated several pyroclastic density currents (PDCs; Nakada et al., 1999a; Sakuma et al., 2008). The flows were estimated to have travelled at 200 km hr^{-1}, up to 5.5 km down the Oshigadani Valley (Yamamoto et al., 1993; Takarada et al., 2013). All in all, pyroclastic flows buried and/or burned approximately 800 buildings, and debris
180 flows destroyed a further ~ 1,700, and in the summer of 1991 the number of evacuated persons exceeded 11,000 (Nakada et al., 1999a). The Committee of Survey and Countermeasure on Lava Dome Collapse at Mt. Unzen advises that the risk of collapse of lobe 11 is high, an exclusion zone remains active to the E of the summit and access to the lava dome is strictly limited. Data from electro-optical distance measuring instruments suggest that the lobe has moved 1 m in 14 years (measurements from 1997-2011), and recent observations from ground-based synthetic aperture radar show the development
185 of a shear fracture (Kohashi et al., 2012). Therefore, a block-and-ash flow is likely, particularly after large regional earthquakes. The current uncertainty of stability of the dome at Mt. Unzen, particularly after seismic activity, has led to recent field campaigns and mechanical studies of the dome material (e.g. Cordonnier et al., 2009; Hornby et al., 2015). Movement of lava domes due to such tectonic activity is essentially superficial, meaning the issue can be considered as a uniaxial problem, and tested as such (e.g. Quane and Russell, 2005).

190 ## 2 Materials and methods

2.1 Sample selection

Mt. Unzen lava dome is made up of porphyritic, dacite (~ 63 wt.% SiO_2) lava blocks which typically have large (> 3 mm) and abundant (> 25 vol.%) plagioclase phenocrysts, along with lesser amounts of amphibole (~ 5 vol.%), biotite (~ 2 vol.%) and quartz (~ 2 vol.%) phenocrysts and microphenocrysts set in a partially crystalline (~ 50 vol.%) groundmass of

195   plagioclase, pyroxene, quartz pargasite, and Fe–Ti oxides in a rhyolitic interstitial glass (Nakada & Motomura 1999; Wallace et al. *in review*). However, as the dome was formed both exogenously and endogenously the microstructure of these blocks varies considerably. Furthermore, lasting heat sources and ongoing fumarolic activity have led to local thermal and hydrothermal alteration of the dome (Almberg et al., 2008). This heterogeneity calls for a variable sample suite to represent the dome material, and to constrain the processes of deformation and cooling that occurred throughout lava dome formation,

200   that influences its current structural stability.

In this study, 9 samples were selected with different properties. Samples UNZ-1, 2, 4, 5, 7, and 8 were collected from easily accessible, June 1993 block–and–ash flow deposits in the Minami–Senbongi area, north–east of the spine; UNZ-13 was collected from the May-August 1991 deposits in the restricted area of the Mizunashi River, east of the spine (see Fig. 1b). These rocks were collected as they represent the freshest (unaltered) materials that originate from dome collapse events

205   during eruption, prior to any chemical alteration (e.g., Cordonnier et al., 2008). Sample UNZ-11 was collected on lobe 11 of the dome, selected as it showed signs of hydrothermal alteration (crusted, white and friable). UNZ-12 was collected on the dome, just east of the lava spine, and was chosen specifically for its reddish colour which suggested thermal alteration and oxidation. Each sample block was then cored to make multiple 20 mm diameter cylindrical cores, cut, and then ground parallel to 40 mm in length (Fig. S1) to maintain a 2:1 aspect ratio in accordance with the ISRM suggested method (IRSM

210   Turkish National Group, 1979).

2.2 Sample characterisation and preparation

2.2.1 Geochemistry

The geochemical composition of the interstitial glass in sample block UNZ-4 was determined using a Cameca SX–5 Field Emission Electron Probe Microanalyser (EPMA) at the University of Oxford. A variety of standards were used to calibrate

215   the spectrometers, including Wollastonite for Ca, and Albite for Al, Na and Si. Secondary reference standards, of which the exact chemistry was known, were utilised for better precision and accuracy. These were Labradorite and kn18 glass (comendite obsidian, Kenya), used as the chemistries were similar to those of the Mt. Unzen glass sample. Analyses used an accelerating voltage of 15 KeV, a beam current of 6 nA and a defocussed spot size of 10 μm. The data were checked for major element oxides' totals.

220   The bulk geochemical compositions of selected samples were determined in a PANalytical Axios Advanced X–Ray Fluorescence Spectrometer (XRF) at the University of Leicester (using fused glass beads prepared from ignited powders). Sample to flux ratio was kept at 1:5, 80% Li metaborate: 20% Li tetraborate flux. Results are quoted as component oxide weight percent and re–calculated to include LOI (loss–on–ignition).

2.2.2 Porosity

225   The porosity and character of the pores (i.e., whether connected or isolated) was assessed using an AccuPyc 1340 helium pycnometer from Micromeritics. Firstly, height (h; in m), radius (r; in m) and mass (m; in kg) were recorded for each cylindrical core sample, providing a constraint on sample density (ρ_s; in kg/m^3):

$$\rho_s = {}^m\!/_{\pi r^2 h},\tag{3}$$

Secondly, the solid density of the rocks (ρ_0) was constrained by measuring the mass and volume of a powdered lump from

230   each rock in a pycnometer; from these measurements, the total porosity of each rock could be estimated via:

$$\varphi_T = 1 - ({}^{\rho_s}\!/_{\rho_0}),\tag{4}$$

To constrain the fraction of isolated pores in the rocks, the skeletal volume ($V_{skeletal}$; in m^3) of each core was measured in the pycnometer. The porosity connected to the outside of the sample (henceforth termed connected porosity), φ_O, could then be calculated via:

235

$$\varphi_O = 1 - \left(\frac{V_{skeletal}}{\pi r^2 h}\right),$$ (5)

and isolated porosity, φ_i, via:

$$\varphi_i = \varphi_T - \varphi_O,$$ (6)

The porosity determination was used to omit outliers from any sample block to ensure that the rocks of a given porosity were tested and compared to one another.

2.2.3 Microstructures

240

Thin sections of UNZ- 4,11,12 and 13 were prepared with a fluorescent dyed epoxy; selected as they cover a vast range of sample diversity; including both the lower and upper bounds of porosity, and collection site. Images were acquired using a DM2500P Leica microscope in plane–polarised light. To further constrain the microstructures of each sample block, backscattered electron (BSE) images were taken of each sample using a Philips XL30 tungsten filament scanning electron microscope (SEM), equipped with an energy–dispersive X–ray spectrometer (EDS), and a Hitachi TM3000 SEM at the University of Liverpool. Stubs of the samples were set in epoxy, polished and carbon coated, before being imaged in the Philips XL30 at a working distance of 13±0.1 mm using a 20 kV beam voltage, a 60–90 μA beam current and a spot size of 5. Thin sections of the samples were imaged with the Hitachi TM3000 using a 15 kV beam and 10 mm working distance.

245

2.2.4 Thermal Analysis

250

To constrain the conditions at which to carry out the high temperature uniaxial tests, we evaluated the softening point of the Mt. Unzen dome rock using a Netzsch 402 F1 Hyperion thermomechanical analysis (TMA) at the University of Liverpool. Under a 20 mL.min^{-1} argon flow, a 6.37 mm tall, 5.87 mm wide, cylindrical sample of UNZ-8 was placed under a constant load of 3 N and heated at 10 ˚C/min to 1100 ˚C. The softening point of the material was found as the temperature at which the applied load counteracts sample expansion by inducing viscous flow (and sample shortening) during heating. This was detected at 824.6 °C, 80.6 minutes into the measurement (Fig. S5). An experimental temperature of 900 °C was selected as, being well above the softening point, this is high enough to allow for flow to occur on the timescales under investigation. This chosen temperature is close to the magmatic temperature (850–870 °C) constrained to have followed mixing (Venezky and Rutherford, 1999) and above the glass transition of Unzen spine material (790 °C) measured by differential scanning calorimetry at a rate of 10 °C.min^{-1} (Wallace et al. *in review*), though the temperature profile within the conduit and dome during emplacement is poorly constrained.

255

260

2.2.5 Thermal stressing

Selected cores of pristine material were thermally stressed in a Carbolite box furnace to examine the effects of experimentally induced heating–cooling cycles on the residual strength of rock cores. Cores were subjected to heating at 4 °C min^{-1} followed by 1–hr dwell at 900±3 °C (sample temperature) and cooling at 4 °C min^{-1}. The density and porosity of each sample were measured before and after thermal stressing, and the products were further subjected to uniaxial compressive strength tests.

265

2.3 Uniaxial compression experiments

Uniaxial compressive strength tests were carried out using a 50 kN 5969 Instron benchtop press and a 100 kN Instron 8862 uniaxial press with a three–zone, split cylinder furnace using the parallel plate method in the Experimental Volcanology and Geothermal Research Laboratory at the University of Liverpool (Fig. 2). Experiments were carried out both at ambient temperature (~20 °C) and at high temperature (900 °C, using a heating rate of 4 °C min^{-1}). Tests were conducted at constant strain rates of 10^{-1}, 10^{-3} or 10^{-5} s^{-1} (see Table 1 for the range of experimental conditions). The apparatus monitored the applied load and piston extension at 10–1000 Hz (depending on set experiment rate) and the Bluehill® 3 software was used to compute data and calculate strain (ε) and compressive stress from the input sample dimensions. [Note: all mechanical data have been corrected for the compliance of the setup, quantified via Instron procedures that monitor length changes due to loading of the pistons in contact with one another]. The end of each experiment was defined by either (1) in the case of viscous flow, when there was a constant stress recorded for a significant amount of time (>1 hour), or (2) in the case of brittle behaviour, a stress drop exceeding 20% of the monitored peak stress achieved, highlighting that failure had occurred. Repeat experiments were performed on samples with a similar porosity (i.e., within 1% of the other sample tested) at various conditions to verify findings.

2.3.1 High temperature experiments

Prepared cores were placed upright in between the pistons of the press; the furnace was closed around the sample which was heated at 4 °C min^{-1} to 900±3 °C (sample temperature); a K–type thermocouple was left in contact with the sample at all times and the temperatures of the top, middle and bottom zones of the furnace were monitored throughout the experiment. Following thermal equilibration for 1 hour at target temperature, the piston was then brought into contact with the sample at low load (< 30 N), and the temperature of the sample was read from the thermocouple. A stepped strain–rate experiment (at 10^{-6} then 10^{-5}, 10^{-4} and 10^{-3} s^{-1}) was first carried out to constrain the viscous–brittle transition of the material and inform subsequent testing at unique strain rates. Tests at unique strain rates were then carried out at 10^{-3}, 10^{-4}, 10^{-5} s^{-1}, after which, the samples were cooled to ambient temperature at 4 °C min^{-1}.

2.3.2 Ambient temperature experiments

Ambient temperature experiments were carried out on all collected sample blocks. Prepared cores were placed upright between the pistons where they underwent compressive tests at various strain rates until failure. The thermally stressed samples were tested at a strain rate of 10^{-3} s^{-1}, whereas the remaining pristine specimens were axially loaded at strain rates of 10^{-1}, 10^{-3}, or 10^{-5} s^{-1} until failure (see Table 1).

2.3.3 Treatment of data

The strain at failure for these samples was selected using a semi–automated script which identified the strain value at peak stress. The static Young's modulus was calculated for each experiment that exhibited a brittle response (e.g. after Heap et al. 2014a) as the linear slope of the stress–strain curve via an automated script. To ensure that only the linear portion was selected, points within 10% of the maximum slope were considered to define the Young's modulus for that sample (Fig. S6), minimising the potential contribution of mechanical data obtained during crack closure (during initial loading) and during strain hardening (beyond the onset of dilation).

For samples that demonstrated a viscous response, the apparent viscosity (η_a; in Pa.s) was calculated using Gents' (1960) equation developed for the parallel–plate method, given the absence of slip along the sample/piston interfaces:

$$\eta_a = \frac{2\pi F h^4}{3V\dot{\varepsilon}(V+2\pi h^3)},$$ (7)

305   where F (N) is the applied force on the sample; h (m) is the height of the sample; V (m^3) is the initial volume of the sample, assumed constant, and $\dot{\varepsilon}$ (s^{-1}) is the applied strain rate.

3. Results

3.1 Sample characterisation

3.2.1 Mineralogy and geochemistry

310   Normalised geochemical analysis for bulk and glass geochemistry, obtained by XRF and EPMA respectively, are displayed in Table 2. Optical examination of the samples reveals that they consist of 20–50 % phenocrysts and microphenocrysts of plagioclase (> 25 vol.%), amphibole (~ 5 vol.%), biotite (~ 2 vol.%) and quartz (~ 2 vol.%) (Fig. 3), where plagioclase and amphibole are the largest of the phenocrysts, and are generally greater than 3 mm. These phenocrysts and microphenocrysts are set in a partially crystalline (~ 50 vol.%) groundmass containing microlites of plagioclase, pyroxene, quartz, pargasite,
315   and Fe–Ti oxides in a peraluminous rhyolitic interstitial glass (as described in Cordonnier et al. 2009). Cristobalite is occasionally observed as pore infills (also recorded by Nakada and Motomura, 1999). The bulk chemistries of samples UNZ-11 and UNZ-12 (deemed visually altered) have slightly more (1.1–1.4 wt.%) SiO$_2$ and slightly less (0.55–0.63 wt.%) CaO than UNZ-4, whilst potassium and sodium concentrations are almost identical.

3.2.2 Rock porosities

320   The total porosities of the samples determined by helium pycnometry measurements range from 0.10–0.32 (Table 3); a scatter which has previously been studied in an investigation of rock frictional properties (Hornby et al., 2015) and which is consistent with field measurements of Mt. Unzen dome products (Kueppers et al., 2005). The pores of the denser products, notably UNZ-4 and UNZ-12, are fully connected, whereas the higher porosity blocks contain a portion (0.01–0.02) of isolated pores. The small standard deviation for the connected, isolated and thus total porosity of the rocks ensures the
325   comparability of mechanical data obtained on samples with similar porosities during repeats.

3.2.3 Microstructures

Microstructural examination can be used to assess any pre–existing anisotropy or fabrics in the lavas. Photomicrographs along with SEM images, of a selected group of samples (UNZ-4,-11,-12,-13) can be seen in Figure 3. These samples are shown due to their contrasting nature, covering the span of textures studied here: UNZ-11 and UNZ-12 are visually altered
330   samples; UNZ-13 has a different pore anisotropy than UNZ-11, and UNZ-4 is a typical product of the block–and–ash flow and is representative of the remaining samples tested. The images in Figure 3 show the original materials, orientated so that the direction of principal stress, σ$_1$, applied to the cores prepared of each rock would be in the vertical direction.
It is evident from Figure 3 that the pores in the Mt. Unzen dome rock samples are preferentially elongate. In some cases, the elongation has a visually preferred orientation (e.g. UNZ-11,-13), while in others it is unsystematic (e.g. UNZ-4,-12). In
335   UNZ-11 vesicles, and microlites, appear to bottleneck around phenocrysts in a horizontal direction (i.e., perpendicular to σ$_1$ imposed in the experiments), whereas in UNZ-13 their alignment is vertical (i.e., parallel to σ$_1$), indicating a sense of shear in those directions. UNZ-4,-11, and -13 have significant number of larger pores (>1 mm) when compared to UNZ-12, and across the shown sample set, these larger pores appear as pressure shadows around the phenocrysts (e.g. see McKenzie and

Holness, 2000). Fractures are only clearly visible in UNZ-4, this is most likely due to higher abundance and larger fracture

340 widths in this sample, allowing them to be visible in both thin section and BSE images. The fractures appear to connect pores via the tip of their major axis.

The groundmass of UNZ-12 contains a scaly–textured quartz polymorph that appears to have filled vesicles. Common quartz polymorphs seen at Mt. Unzen, and other domes across the world (e.g. Mt. St. Helens; Voight et al. 1981), are cristobalite precipitates, formed from hydrothermal activity (Nakada and Motomura, 1999; Voight et al., 1981, 2009; Yilmaz et al., *in*

345 *review*). This silica deposit has filled a considerable amount (~ 50 %) of the vesicles in UNZ-12, reducing its porosity (Fig. 3c). Although the polymorph is a sign of alteration, in the highest magnification BSE image, some glass appears to have remained vitreous between quartz polymorph areas. Similarly, in UNZ-11, neither the phenocrysts nor the groundmass show evidence of alteration (Fig. 3b,c).

In UNZ-12 the phenocrysts are visually more abundant (> 20 vol.%) than in the other specimens (Fig. 3). Nakada and

350 Motomura (1999a) observed that groundmass crystallinity increased from (33 to 50 vol.%) with decreasing effusion rate, as was the case towards the end of the eruption (Nakada et al., 1995b), consistent with ~ 55 % groundmass crystallinity in the 1994-95 spine (Wallace et al. *in revie*w). These observations are also consistent with the crystal fractions measured in UNZ-12, collected from the near–vent area.

3.2.4 The influence of thermal stressing

355 The skeletal volume, mass and dimensions of each core were measured before and after thermal stressing in order to assess changes in porosity that may accompany microstructural adjustment in the process. Results showed that over the 12 cores subjected to thermal stressing, the change in connected porosity was less than 0.001, which is within the resolution of the method. Thus, it may be said that thermal stressing did not create significantly more pores nor connect isolated vesicles.

3.2 Uniaxial compressive experiments

360 ### 3.2.1 Mechanical response of Mt. Unzen dome rocks

Uniaxial compressive strength tests were conducted on 66 cores at ambient temperature. For those samples which had a brittle response to uniaxial compression, the failure process can be segregated into 4 stages (Hoek and Bieniawski, 1965; e.g. Brace et al., 1966; Scholz, 1968; Heap et al., 2014a). An initial build–up of stress has been attributed to the closure of micro–cracks perpendicular to σ_1, this is the initial convex segment on the stress–strain curve (e.g. Fig. 4a,b). The second, linear

365 increase in stress is recoverable and has been attributed to dominantly elastic deformation. Strain hardening, marks the onset of micro–fracturing that imparts permanent, non–recoverable damage, causing deviation from the linear elastic regime during loading (seen as the concave section of the stress–strain curve; Fig. 4a,b). Finally, a peak in stress is reached, followed by an abrupt stress drop, this is associated with through–going fracture propagation and coalescence before macroscopic failure is reached. This behaviour is seen in the stress–strain curves (Fig. 4a,b, Fig. S3, S4) of all samples

370 deformed in the brittle regime, be it at ambient temperature (for all strain rates) or at high temperatures (for faster strain rates; see section 3.2.2).

The strength of the rocks was observed to decrease with porosity (Fig. 5a). The range of strength of dense rocks is higher than porous rocks. We observe that rock strength increases with applied strain rates at all porosities, although this effect is more pronounced for dense rocks. The data suggest that the rocks deemed altered (UNZ-11, UNZ-12) are not weaker, but

375 indeed stronger than pristine rocks with equivalent porosities (see circled data points in Fig. 5a).

The overlap between the datasets obtained for thermally stressed and as-collected samples suggests that thermal stressing did not impart significant damage or mineralogical changes (if any) to modify the strength of these rocks (Fig. 5). Yet, a closer

look at the mechanical data suggests that the initial increase in stress with strain is more pronounced for the thermally stressed samples than for their pristine equivalent (Fig. 4c), indicating that thermal stressing has caused the opening of micro–fractures, dislocating the rocks slightly in the process.

3.2.2 Rheological response of Mt. Unzen dome lavas

The mechanical data of lavas show a wider range of behaviour than those obtained on rocks at ambient temperature (Fig. 4a,b). At the faster strain rate of 10^{-3} s^{-1}, the samples responded brittlely, like at room temperature; stress accumulation eventually led to failure and significant stress drop, although not as rapid as the stress drops monitored during failure of cold lavas (e.g. Fig. 4a). The samples deformed at lower strain rates of 10^{-5} s^{-1} and 10^{-4} s^{-1} underwent viscous responses, and thus have differently shaped stress–strain curves. Initially, they exhibit only a mildly convex stress build–up (more obvious in the brittle examples), but then deformation is dominated by a stress relaxation phase which results in a levelling of the stress to a steady value as strain amasses. This represents the viscous flow of the suspension, and as such its apparent viscosity can be calculated from the mechanical data.

The evolution of apparent viscosity is strain–rate dependent as shown by the stepped strain rate experiment (Fig. 6). An increase in the strain rate resulted in an order of magnitude decrease in viscosity- a thixotropy of similar magnitude as that described for highly crystalline magmas in Lavallée et al. (2007). In this experiment, deformation at low strain rates of 10^{-6} s^{-1}, 10^{-5} s^{-1} and 10^{-4} s^{-1}, is marked by a non-linear increase in apparent viscosity (upon stress relaxation) and plateauing to a constant value for each strain–rate step; this value decreased with increase of the applied strain rate (Fig. 6). Deformation was pervasive (i.e., ductile), which, being above Tg, suggests that it dominantly occurred via a viscous response. At 10^{-3} s^{-1}, however, the apparent viscosity plummeted as the sample underwent failure along a localised fault, evidencing a transition into the brittle regime (Fig. 6b).

When in the brittle regime (at strain rates of 10^{-3} s^{-1}) the sample suite tested reached peak stresses of ~ 20–80 MPa (Fig. 7a) and strength decreased inversely with porosity. These high temperature experiments were more repeatable than those carried out at ambient temperature, samples within a ~ 1 % porosity range failed within ~ 2 % of each other at low porosities (< 0.20) and within ~ 5 % of each other at high porosities (> 0.20), whereas at ambient temperatures a variation of ~ 60 % is observed in the lower porosity regime (Table 1).

When a strain rate of 10^{-4} s^{-1} was applied some of the samples reached peak stresses between ~ 10 and 35 MPa (Fig.7b), before relaxing the stress through substantial strain. Here, instead of solely brittle behaviour, the lavas display a transitional response to strain. At first, the response was viscous, then, in some samples, after a certain amount of strain, fracturing occurred, leading to macroscopic failure. Samples that did not fracture continued to flow viscously with increasing strain, with a component of strain hardening, similar to that seen by Kendrick et al. (2013b). Samples that were subjected to a strain rate of 10^{-5} s^{-1} had a fully viscous response over the strain rates tested (Fig. 7c). Remarkably, the peak stresses of samples tested at 10^{-4} and 10^{-5} s^{-1} were seemingly independent of porosity (Fig. 7d).

The apparent viscosities calculated from the responses at 10^{-5} and 10^{-4} s^{-1} show an initial increase (due to relaxation in the first 0.7% strain) and levelling to within a narrow range (see Fig. 8a,b). For a given strain rate, we note a small range of apparent viscosities, but importantly, no systematic change in viscosity as a function of sample porosity (within the range tested; Fig. 8c).

These results indicate that the transition in deformation mode from macroscopically ductile to brittle behaviour is straddled by our experiments in the range 10^{-5} to 10^{-3} s^{-1}.

4. Interpretation of dome rock mechanics

4.1 Mechanical responses of rocks and lavas in the brittle regime

The experimental findings presented here suggest that the mechanical response of lavas and rocks is similar, but important differences remain. Experiments carried out on rocks at ambient temperature and all strain rates, and on lavas at high temperature and high strain rates of 10^{-3} s^{-1}, resulted in brittle behaviour. However, there are significant differences in the mechanical response between the two (Fig. 4). (1) We noted a shorter convex portion at high temperature at the onset of the stress-strain curve (Fig. S3), which we attribute to a narrowing of pre-existing cracks at high temperature (due to thermal expansion of the materials with heating; e.g., Fig. S5), resulting in a smaller extent of crack closure during initial loading of samples at high temperature; (2) Most high-temperature samples have a shallower linear portion of stress-strain build-up, which we hypothesise may reflect a contribution of viscous deformation upon loading; and (3) we observed a less angular concave down portion of the stress–strain curve, which we attribute to more pervasive deformation (as seen by longer strain to failure; Fig. 9) and micro–fracturing leading to failure. The exception to these findings is in the highest porosity sample, UNZ-7, where there appears to be no significant change in shape between high and ambient temperature experiments (see Fig. S3, S4). But it remains that at higher temperature, lavas are stronger (by 10–40 MPa; Figs 4–9) than their rock equivalents at ambient temperature. Before delving in their differences (section 4.1.4), we will first interpret the results on the strength (section 4.1.2) and young's modulus (section 4.1.3) of porous rocks at ambient temperature

4.1.2 The effect of porosity on material strength

From the results of the uniaxial compressive experiments it is evident that porosity is a major control on the maximum stresses reached by the samples. Previous studies on volcanic rocks (Al-Harthi et al., 1999; Heap et al., 2014a, 2014b, 2016b; Schaefer et al., 2015) have found a similar correlation. Therefore, it can be said that, to a first order, strength is inversely proportional to the porosity of the rock.

Here, the strength of samples with higher porosities have less scatter than those with lower porosities (Fig. 9a). The microstructures of the samples (Fig. 3) show the porosity of the porous specimens to be dominated by vesicles, while the porosity of the denser samples is dominated by microfractures, which may define a change in the failure mechanism between low and high porosity samples. Given the pore structures, in the higher porosity specimens the behaviour of failure could be described using the pore emanating crack model of Sammis & Ashby (1986), whereas, in the lower porosity experiments, the main failure mechanism could be explained by the sliding wing crack model of Ashby & Sammis (1990). In these lower porosity specimens, the non-systematic orientation of microfractures could be responsible for the large scatter in strength. The transition in the preference of fracture nucleation site from pore to crack is likely to be gradual and dependent on the pore network architecture of a suite of samples; in these Mt. Unzen samples it is found at a porosity of ~ 0.2. Other studies have also alluded to such a transition when studying permeability, finding a transition from crack-dominated to pore-connectivity dominated regime of fluid flow at values of ~ 0.14 (Farquharson et al., 2015), 0.155 (Heap et al., 2015b), 0.105–0.31 (Kushnir et al., 2016), ~ 0.15 (Eggertsson et al., *in review*), and 0.11–0.18 (Lamur et al., 2017).

Samples UNZ-11 (porosity: 0.30) and UNZ-13 (porosity: 0.32) both have elongated vesicles. The cores were cut so that the vesicles were either perpendicular or parallel to the applied principal stress, σ_1, for UNZ-11 and UNZ-13, respectively. As the porosities of the two rocks are comparable, and as they have similar strengths, it can be noted that, for Mt. Unzen, the orientation of a vesicle does not have a major influence on the strength of a rock. Although recent findings indicate that the orientation of a pore has a dominant effect on a rock's strength (Bubeck et al., 2017; Griffiths et al., 2017) we do not observe that for the porous network architecture of the Mt. Unzen rocks tested here. However, we do note that UNZ-11 undergoes a

higher strain to failure (Fig. 9b) and thus lower Young's Modulus (Fig. 9c) than UNZ-13; as their porous structure is similar, we turn to their mineral constituents. UNZ-11 had been collected from the dome, owing to its altered look (crusted, white and friable; see Fig. S1). Although the geochemical analysis suggests a certain degree of alteration, we did not observe any alteration of the main mineral phases nor deposition of any secondary mineral phases in our textural analysis, yet the latter
460   may still have in–filled fine cracks and it is possible that the glass devitrified as a result of hydration, which may affect the mechanical response. For instance, UNZ-12, which was also selected for its altered and oxidised appearance, have less Mg, Ti, and Fe (attributed by Goto et al. (2008) to the production of haematite from oxidisation), a higher degree of microfractures and a far more complex microstructure than similar rocks; yet, it is the strongest rock investigated here. Thus, future studies may benefit from an in-depth study of rock strength as a function of porosity and alteration.

465

4.1.3 Static Young's Modulus

At ambient temperatures, the static Young's modulus decreases from > 15 GPa to < 5 GPa with increasing porosity (Fig. 9c). This is an indication that samples with lower porosities were stiffer than those with higher porosities. However, there were outliers to the data trend, UNZ-13 and UNZ-2 (with average porosities of 0.32 and 0.13, respectively) have higher (> 5 GPa)
470   Young's Moduli than other rocks with similar porosities (see Table 1). This suggests that these samples are stiffer than the other specimens tested, and indeed those experiments reached unusually high peak stresses at relatively low strains to failure. This is intuitive as the pores in UNZ-13 are parallel to the principal stress and are therefore harder to deform, as for UNZ-2, it has the highest number of isolated pores (Table 3) which are spherical (i.e. low Ca) (see Fig. S2) and so act as rigid bodies. The naturally altered samples, tested at similar conditions, exhibited Young's Moduli trends like those of comparable fresh
475   rocks (Fig. 9c).

Lavas deformed at 900 °C, but which failed in the brittle field (i.e. at a strain rate of 10^{-3} s^{-1}) have systematically lower (~ 5–10 GPa) Young's moduli. It is this malleability that allows the lava to be deformed to higher strains before macroscopic failure (Fig. 9b), an observation recognised in Schaefer et al., (2015) in tests on basaltic lavas.

In addition, thermally stressed samples have slightly lower (~ 0.5–1.5 GPa) Young's moduli than their unstressed
480   equivalents, as previously noted in dacites from Mt. St. Helens (Kendrick et al., 2013a). This highlights a potential change in porosity distribution that was not recognised by other means (e.g. total porosity, strength).

4.1.4 The effect of temperature on sample strength

Remarkably, when in the brittle regime at high temperature, samples exhibited strengths ~ 10–40 MPa greater than at ambient temperature. This may be attributed to the way the samples respond to stress at higher temperatures. First, upon
485   heating a rock, it expands, which may partially close pre-existing micro-fractures, thus modifying the resultant elastic response of the material (see section 4.1.1). Moreover, at 900 °C the presence of interstitial melt in a sample allows for considerably more strain than if it were deformed at ambient temperature (when in a solid, glassy state). The initial strain upon loading would be accommodated by both an instantaneous and a delayed (relaxation) elastic response (e.g. Dingwell and Webb, 1989) and perhaps minor micro–crack closure (e.g. Heap et al., 2014a), before the onset of viscous (e.g. Lavallée
490   et al., 2007) and crystal plastic (e.g. Kendrick et al. 2017) deformation that results in permanent deformation (and barrelling of the sample). Thus, at higher temperatures, more strain is accommodated upon loading than at ambient temperature (Fig. 6a), leading to higher strain to failure (Fig. 9b) and lower Young's Moduli than their rock counterparts (Fig. 9c). The Young's Moduli for lavas undergoing failure at high temperature are rate–dependent, perhaps as they undergo further stress dissipation by viscous relaxation in the melt.

495   A similar increase in strength with temperature was also noted in basaltic rocks from Pacaya volcano (Schaefer et al., 2015). There, the authors attributed the increase in strength of the glass–poor rock to the closure of micro–cracks (likely formed upon cooling after their eruption) due to thermal expansion, a process that equally occurs in Mt. Unzen dome rocks. Rocks may also become weaker from thermal stressing, this can be due to crack initiation (Heap et al., 2016a), or alteration, via processes such as decarbonation and dehydroxylation (Heap et al., 2012, 2013a, 2013b). A recent study by Eggertsson et al.,

500   *in review*, found that samples that hosted microfractures (like Mt. Unzen dome rock) were not affected by thermal stressing, while those that showed a trivial fraction of pre-existing micro-fractures were more readily fractured through thermal stressing and as a result became more permeable.

5. Rheology of dome lavas

5.1 Viscosity of dome lavas

505   The style of an eruption – effusive vs explosive – depends on the rheological response of magma (Dingwell, 1996). The urge to understand the alarmingly variable nature of volcanoes, and recent advances in experimental capabilities and computational modelling, have encouraged the community to focus efforts on the development of two and three–phase models of magma rheology (e.g. Lejeune and Richet, 1995; Caricchi et al., 2007; Lavallée et al., 2007; Costa et al., 2009; Mueller et al., 2011b; Truby et al., 2015). Truby et al., (2015) combined two, two–phase flow models (considering

510   melt+crystal and melt+gas bubbles) to elaborate a three–phase model of magmatic suspensions, further tested against a set of controlled analogue laboratory data. Their model shows that while the addition of crystals increases the viscosity of a suspension, leading to a shear thinning rheology, the addition of gas bubbles (which can deform during shear) has variable consequences. Depending upon the initial crystal volume and maximum packing fraction of those crystals, the addition of gas bubbles may result in a further increase in viscosity or, in other cases, a levelling or a decrease in the apparent viscosity

515   of the suspension. Their model suggests that the addition of bubbles to lavas with high normalised crystal fractions, like those seen in volcanic domes, would likely decrease the viscosity of the suspension. However, here, the data show that the presence of vesicles (between 0.09 and 0.33) in dome lavas may not necessarily influence the apparent viscosity. We advance that this could be due to the high connectivity of the pores present in dome lavas, which allows efficient outgassing, thus the gas cannot act as an isolated phase that can pressurise during shear. Thus, it may be that lavas hosting permeable

520   porous networks may have mostly porosity–independent apparent viscosities (at least across the range examined here), as suggested by Lavallée et al. (2007). Current models relating porosity to viscosity, simply account for the presence of isolated gas bubbles via a capillary number, to calculate the apparent viscosity of a multi–phase suspension (e.g. Rust and Manga, 2002; Llewellin and Manga, 2005; Truby et al., 2015). However, this result highlights important shortcomings to the modelling of shallow magmas, where porous networks tend to develop connectivity, especially in sheared crystal–bearing

525   lavas (e.g. Laumonier et al., 2011). This connectivity controls outgassing, and thus pressure build–up or release, which is responsible for rheological variations in magma and therefore eruption style (effusive vs explosive). Our findings suggest that we need to revise three–phase models to account for gas flow through evolving, deformable bubbles, that may also be connected, in order to constrain the apparent viscosity of magmas in lava domes and other open–system settings.

5.2 Failure criterion for porous lavas

530   During magma ascent, the strain rate, which is proportional to effusion rate (e.g., Goto 1999), plays a key role in determining whether the response of magmas and lavas is that of a solid, or liquid (Webb and Dingwell, 1990). The distinction between these rheological regimes can be made using the Deborah number (Eq. 2). This dimensionless ratio of the relaxation timescale of the melt (Eq. 1) and the observation timescale can be rewritten as:

$$De = {}^{\eta_m}/_{G_\infty} t_{obs},\qquad(8)$$

535 where the observation time, $t_{obs,}$ is the inverse of the strain rate of magma deformation, $\dot{\varepsilon}_{exp}$. Thus Eq. 8 can be rewritten as:

$$De = \dot{\varepsilon}_{exp}\,\eta_m\,/\,G_\infty,\qquad(9)$$

Magmatic suspensions, like those described in this study, are non–Newtonian materials with a shear thinning response (Caricchi et al., 2007; Lavallée et al., 2007; Cordonnier et al., 2009; Avard and Whittington, 2012; Vona et al., 2013), hence their viscosity is strain rate dependent. It has previously been described that the peak stress, σ, shares a power law
540 relationship with strain rate, $\dot{\varepsilon}_{exp}$, via:

$$\sigma = k\dot{\varepsilon}_{exp}{}^{b},\qquad(10)$$

where k is the flow consistency index (in Pa.s) and b is the flow behaviour index, describing the rheology of the fluids (Ostwald, 1925; Lavallée et al., 2007). For Newtonian bodies $b = 1$, but for shear thinning suspensions, b decreases below 1 (Caricchi et al., 2007) and reaches a minimum of $b = 0.5$ for crystal–rich materials (Lavallée et al., 2007; Cordonnier et al.,
545 2009). In the present study the Mt. Unzen dome material tested at 900 °C, by fitting a power law to the peak stress–strain curve we obtained Oswald constants of $k = 1653$ and $b = 0.5$ (Fig. 10a). So, we can rewrite Eq. 9, using Eq. 10, to obtain:

$$De = \frac{(\sigma/_k)^{1/_b}\eta_l}{G_\infty},\qquad(11)$$

which permits the representation of the Deborah number of material failure as a function of strength (which was shown to be dependent on porosity), for a given temperature (and thus interstitial melt viscosity). For our samples, the interstitial melt
550 viscosity can be estimated at $10^{9.42}$ Pa.s (using its chemistry and experimental temperature as an input parameter in the GRD viscosity calculator (Giordano et al., 2008)). In Figure 10b, we present the data using symbols that illustrate the response of the samples; whether it flows or fails near–instantaneously, or after some amount of strain. This analysis demonstrates that the critical Deborah number, $De_{c,}$ which indicates rupture, of dome lavas from Mt. Unzen decreases by almost one order of magnitude over a 0.35 difference in porosity; from ~ 2×10^{-4} in the densest sample measured to 8×10^{-5} in the most porous,
555 following the trend: $De_c = -5.1\times10^{-4}\varphi + 2.11\times10^{-4}$ (Fig. 10b). Such a magnitude is proportional to the strength decrease of material as a function of porosity (see Fig. 9a and Paterson and Wong, 2005 for a discussion), and thus relates the porosity to the ability of lavas to rupture. Thus both, the addition of crystals (as seen by the fact that De_c of dense dome lavas is reduced by over one order of magnitude compared to that suggested by Dingwell and Webb, (1990)) and vesicles (as shown by the above equation) contributes to an increased brittleness of lava during ascent and eruption at lava domes and in many other
560 eruptive scenarios.

6. Implications for volcanic scenarios

The findings observed here help constrain the impact of rheological evolution on lava domes as they erupt and cool following emplacement. The rheology of magma has a fundamental influence on the style of a volcanic eruption, be it explosive or effusive (Dingwell, 1996; Gonnermann and Manga, 2007). Understanding how magmas respond to changes in
565 petrology, stress and eruptive shearing conditions that occur during ascent in conduit may help to enhance models that aim to predict volcanic activity. The work undertaken here constrains the material behaviour of erupting dome lavas and the relics that remain once the lava cools.

As magma crystallises, its apparent viscosity (generally) increases as the melt evolves and an increasing fraction of the suspension becomes solid (with slower diffusivity and lower rate of plasticity than the viscous liquid melt), thus the
570 suspension becomes increasingly solid–like. For crystalline magmas, we would expect De_c to be lower than that for silicate

liquids (*i.e.*, $De_c < 10^{-2}$; e.g., Gottsmann et al., (2009)). Cordonnier et al., (2012a, 2012b) constrained the failure of silicate liquids with different crystal fractions, and they indeed showed that De_c decreases when crystallinity increases. They suggest that De_c linearly decreases from 10^{-2} to 2×10^{-3} between 0 and 60 vol.% crystals. However, the viscosity used to estimate Maxwell's relaxation rate in the De analysis was based on the suspension's apparent viscosity rather than the interstitial melt

575   viscosity. However, to constrain how the addition of crystals shifts the onset of failure of a material whose rheology is well known it is advantageous to consider the pure melt. Given this, an even larger decrease of De_c would be observed (perhaps down to ~ 2.11×10^{-4} as constrained by failure of our densest lavas). Since the strength of material is known to be strongly influenced by the presence of pores (commonly vesicles in volcanic materials) and micro–fractures (e.g., Paterson and Wong, 2005 for a review of material properties in the brittle field), here we demonstrate that the addition of porosity to

580   magma shifts failure to lower strain rates; thus, under constant ascent conditions, magma may undergo failure simply by vesiculation, without the need for any increase in strain rate.

Upon extrusion, dome lava cools, contracts and fractures (Heap et al., 2015a). Here we show that the strength of a dome is reduced upon cooling due to contraction and micro-fracturing, leaving a weaker relic structure. This situation may favour the progressive creep of cooling dome structure, as observed in lobe 11 at Mt. Unzen (Kohashi et al., 2012).

585   Post-emplacement, through time and prolonged exposure to corrosive fluids, dome material may alter (Ball et al., 2015). In this study, the altered rocks tested showed a higher strength than pristine rocks with equivalent porosities. However, previous studies have found that altered volcanic rocks can also be weaker (e.g. Pola et al., 2012). From this distinction we surmise that the structure of the rocks as well as the type of alteration (developing under different conditions in cooling volcanic rocks) may have contrasting effect on the strength of dome lavas. Thus, the data shown here begs for an increased focus on

590   the impact of alteration on volcanic rock strength for improved lava dome structural stability models.

The rate of deformation imposed on dome materials is also an important variable to be considered. In this study, and in others (e.g. Schaefer et al., 2015; Lavallée et al., 2018), volcanic rocks have been shown to withstand higher stresses when deformed at higher strain rates. Previous studies have suggested earthquakes with high ground acceleration have provoked lava dome collapse (Voight, 2000), therefore, it is essential to understand the effect strain rate on the strength of materials.

595   This is of particular importance for Mt. Unzen as it is located in a very seismically active area. Slow, continuous (or recurring stressing cycles) can induce fatigue in a material and brittle creep (e.g. Heap and Faulkner, 2008; Heap et al., 2009; Brantut et al., 2013; Kendrick et al., 2013a; Schaefer et al., 2015) thus weakening the rocks which undergo failure at lower stresses. Thus, over long periods (years) of deformation, such as for lobe 11 at Mt. Unzen, the actual strength of the dome rocks may be lower than those reported here at the lowest strain rate of 10^{-5} s^{-1}). Time-dependent deformation can

600   importantly contribute to catastrophic collapse of volcanic structures (e.g. Mt. St. Helens, Reid et al. 2010). Here we surmise that it is crucial for future failure models of volcanic materials to incorporate the effect of strain rate.

Volcanic structures are made of heterogeneous rocks and lavas, with intricate mineralogical assemblages, textures and fabrics, with variable degrees of coherence; thus, their mechanical response may vary widely. Although here we have only tested material from the 1991–1995 eruption of Mt. Unzen, this study has the potential to be applied to other dome–forming

605   volcanoes of similar composition, crystallinity, and porosity. Additionally, the work can also be applied to parts of larger volcanic edifice dominantly constructed by the accumulation of lavas, which may be prone to collapse (Ball et al., 2015). The work presented here can help constrain the behaviour of lavas and rocks involved in lava dome eruptions. We anticipate that the results will form the basis for more advanced numerical simulations of dome eruption and related hazards.

7. Conclusion

610   Uniaxial experiments carried out at ambient and high temperature (900 °C) on a suite of natural lavas from Mt. Unzen have given significant insight into the behaviour of lava domes, both during extrusion and after emplacement. Ambient

temperature experiments allowed for the investigation of brittle behaviour, and results from these experiments can be applied to cooling domes (and the relics that they leave in the record) volcanic edifice failure. Conclusions drawn from experimentation are as follows:

615   1.   In the brittle regime, strength decreases with increasing pore volume both at ambient and high temperatures;

2.   Magmas deformed in the brittle regime at high temperature are stronger than rocks of equivalent porosity deformed at ambient temperature;

3.   The orientation of a vesicle may not necessarily have a discerning control on the strength of a rock, however it does have an influence on the strains reached at failure and, as such, the Young's Modulus;

620   4.   Thermal stressing did not affect the strength of dome rocks within the conditions tested (< 900 °C and 4 °C.min^{-1}), it did however change the morphology of the stress strain curve, indicating the widening of cracks;

5.   The presence of alteration may have variable effects, sometimes strengthening volcanic rocks;

6.   The strength of rocks and lavas (in the brittle field at high temperature) increases with strain rate;

7.   The viscosity of dome lavas decreased with strain rate (shear thinning) and did not vary with porosity (for the
625   crystallinity studied);

8.   Lavas deformed at high-temperature and strain rates of $> 10^{-4}$ s^{-1} becomes increasingly brittle, and adopt fully brittle response above 10^{-3} s^{-1}; and

9.   The critical Deborah number, De$_c$ of dense dome lavas was found to be ~ 2.11×10^{-4}. It decreases with porosity according to the linear relationship De$_c$ = $-5.1 \times 10^{-4} \varphi + 2.11 \times 10^{-4}$.

630 These results reveal that current stability models of cooling lava domes, like that of lobe 11 at Mt. Unzen, require an integration of the complex nature of the materials. The outcome of this study suggests that, as a primary control on rock strength, porosity heterogeneities must be included when modelling failure mechanisms. As secondary controls, it would also be beneficial to include deformation conditions such as temperature and strain rate. Conclusions drawn from high temperature experiments suggest that current three–phase models may not be fully applicable to dome lavas and other
635 crystal-rich lavas. We suggest a new formulation of the Deborah number that applies to porous, crystal-rich lavas and propose that it may help refine the accuracy of models attempting to describe rheological evolution to explain geophysical data monitored during lava dome eruptions.

Data availability

Supplementary data are available in the Supporting Information "S1" to "S6". Further information can be obtained on
640 request from the corresponding author.

Author contribution

YL and JEK designed the experiments. RC, AJH, TM, JEK, PAW, and JDA carried out the mechanical experiments and physical measurements. PAW collected microprobe data and conducted softening point determination. RC wrote the processing codes, analysed the data, and prepared the manuscript with contributions from all co-authors. All authors
645 contributed to the collection and selection of samples.

Competing interests

The authors declare that they have no conflict of interest.

Acknowledgements

650   RC, JEK, PAW, AJH, TM, JDA, and YL acknowledges funding from the European Research Council (ERC) Starting Grant
on Strain Localisation in Magma (SLiM; No. 306488), JEK was supported by an Early Career Fellowship of the Leverhulme
Trust. PAW acknowledges the NERC ATSC training for providing time to conduct EPMA measurements. Fieldwork was
funded by the DIAWA Anglo-Japanese Foundation (grant number: 11000/11740). The authors would like to thank Prof.
Hiroshi Shimizu for his guidance throughout the study. The AST14DEM used in Fig. 1 was retrieved from the online Data
Pool, courtesy of the NASA Land Processes Distributed Active Archive Center (LP DAAC) and the NASA the Japan
655   Ministry of Economy, Trade and Industry (METI),
(https://lpdaac.usgs.gov/dataset_discovery/aster/aster_products_table/ast14dem_v003#tools)

References

Al-Harthi, A. A., Al-Amri, R. M. and Shehata, W. M.: The porosity and engineering properties of vesicular basalt in Saudi
Arabia, Eng. Geol., 54(3–4), 313–320, doi:10.1016/S0013-7952(99)00050-2, 1999.

660   Almberg, L. D., Larsen, J. F., Eichelberger, J. C., Vogel, T. a. and Patino, L. C.: Comparison of eruptive and intrusive
samples from Unzen Volcano, Japan: Effects of contrasting pressure-temperature-time paths, J. Volcanol. Geotherm. Res.,
175(1–2), 60–70, doi:10.1016/j.jvolgeores.2008.03.020, 2008.

Angelo Heilprin: Mont Pelée and the Tragedy of Martinique: A Study of the Great Catastrophes of 1902, with Observations
and Experiences in the Field, J. B. Lippincott Company., 1903.

665   Ashby, M. F. and Sammis, C. G.: The damage mechanics of brittle solids in compression, Pure Appl. Geophys., 133(3),
489–521, doi:10.1007/BF00878002, 1990.

Ashworth, J. D., Wallace, P. A., Kendrick, J. E., Coats, R., Miwa, T. and Matsushima, T.: Conduit permeability in dilational
and compactional shear zones: a case of Unzen volcano, Japan, in prep

Avard, G. and Whittington, A. G.: Rheology of arc dacite lavas: experimental determination at low strain rates, Bull.
670   Volcanol., 74(5), 1039–1056, doi:10.1007/s00445-012-0584-2, 2012.

Ball, J. L., Stauffer, P. H., Calder, E. S. and Valentine, G. A.: The hydrothermal alteration of cooling lava domes, Bull.
Volcanol., 77(12), 1–16, doi:10.1007/s00445-015-0986-z, 2015.

Barmin, A., Melnik, O. and Sparks, R. S. J.: Periodic behavior in lava dome eruptions, Earth Planet. Sci. Lett., 199(1–2),
173–184, doi:10.1016/S0012-821X(02)00557-5, 2002.

675   Brace, W. F., Paulding, B. W. and Scholz, C.: Dilatancy in the fracture of crystalline rocks, J. Geophys. Res., 71(16), 3939–
3953, doi:10.1029/JZ071i016p03939, 1966.

Brantut, N., Heap, M. J., Meredith, P. G. and Baud, P.: Time-dependent cracking and brittle creep in crustal rocks: A review,
J. Struct. Geol., 52(1), 17–43, doi:10.1016/j.jsg.2013.03.007, 2013.

Bubeck, A., Walker, R. J., Healy, D., Dobbs, M. and Holwell, D. A.: Pore geometry as a control on rock strength, Earth
680   Planet. Sci. Lett., 457, 38–48, doi:10.1016/j.epsl.2016.09.050, 2017.

Calder, E. S., Luckett, R., Sparks, R. S. J. and Voight, B.: Mechanisms of lava dome instability and generation of rockfalls
and pyroclastic flows at Soufrière Hills Volcano, Montserrat, in Geological Society, London, Memoirs, vol. 21, pp. 173–
190., 2002.

Calder, E. S., Lavallée, Y., Kendrick, J. E. and Bernstein, M.: Lava Dome Eruptions, in The Encyclopedia of Volcanoes,
685   edited by H. Sigurdsson, B. Houghton, H. Rymer, J. Stix, and S. McNutt, pp. 343–362, Elsevier., 2015.

Caricchi, L., Burlini, L., Ulmer, P., Gerya, T., Vassalli, M. and Papale, P.: Non-Newtonian rheology of crystal-bearing
magmas and implications for magma ascent dynamics, Earth Planet. Sci. Lett., 264(3–4), 402–419,

doi:10.1016/j.epsl.2007.09.032, 2007.

Cashman, K. V.: Groundmass crystallization of Mount St. Helens dacite, 1980-1986: a tool for interpreting shallow
690   magmatic processes, Contrib. to Mineral. Petrol., 109(4), 431–449, doi:10.1007/BF00306547, 1992.

Cashman, K. V. and Sparks, R. S. J.: How volcanoes work: A 25 year perspective, Bull. Geol. Soc. Am., 125(5–6), 664–690,
doi:10.1130/B30720.1, 2013.

Castro, J. M., Manga, M. and Martin, M. C.: Vesiculation rates of obsidian domes inferred from H2O concentration profiles,
Geophys. Res. Lett., 32(21), 1–5, doi:10.1029/2005GL024029, 2005.

695   Cole, P. D., Calder, E. S., Druitt, T. H., Hoblitt, R., Robertson, R., Sparks, R. S. J. and Young, S. R.: Pyroclastic flows
generated by gravitational instability of the 1996-97 lava dome of Soufriere Hills Volcano, Montserrat, Geophys. Res. Lett.,
25(18), 3425–3428, 1998.

Collombet, M., Wadsworth, F. B., Gurioli, L., Scheu, B., Kueppers, U., Di Muro, A. and Dingwell, D. B.: The evolution of
pore connectivity in volcanic rocks, Earth Planet. Sci. Lett., 462, 99–109, doi:10.1016/j.epsl.2017.01.011, 2017.

700   Cordonnier, B., Hess, K., Lavallée, Y. and Dingwell, D. B.: Rheological properties of dome lavas: Case study of Unzen
volcano, Earth Planet. Sci. Lett., 279(3–4), 263–272, doi:10.1016/j.epsl.2009.01.014, 2009.

Cordonnier, B., Caricchi, L., Pistone, M., Castro, J. M., Hess, K., Gottschaller, S., Manga, M., Dingwell, D. B. and Burlini,
L.: The viscous-brittle transition of crystal-bearing silicic melt: Direct observation of magma rupture and healing, Geology,
40(7), 611–614, doi:10.1130/G3914.1, 2012a.

705   Cordonnier, B., Schmalholz, S. M., Hess, K. and Dingwell, D. B.: Viscous heating in silicate melts: An experimental and
numerical comparison, J. Geophys. Res. Solid Earth, 117(2), 1–13, doi:10.1029/2010JB007982, 2012b.

Costa, A., Caricchi, L. and Bagdassarov, N.: A model for the rheology of particle-bearing suspensions and partially molten
rocks, Geochemistry, Geophys. Geosystems, 10(3), 1–13, doi:10.1029/2008GC002138, 2009.

Deubelbeiss, Y., Kaus, B. J. P., Connolly, J. and Caricchi, L.: Potential causes for the non-Newtonian rheology of crystal-
710   bearing magmas, Geochemistry, Geophys. Geosystems, 12(5), 1–22, doi:10.1029/2010GC003485, 2011.

Dingwell, D. B.: Volcanic Dilemma: Flow or Blow?, Science (80-.)., 273, 1054–1055, doi:10.1126/science.273.5278.1054,
1996.

Dingwell, D. B. and Webb, S. L.: Structural relaxation in silicate melts and non-Newtonian melt rheology in geologic
processes, Phys. Chem. Miner., 16(5), 508–516, doi:10.1007/BF00197020, 1989.

715   Dingwell, D. B. and Webb, S. L.: Relaxation in silicate melts, Eur. J. Mineral., 2(4), 427–449, doi:10.1127/ejm/2/4/0427,
1990.

Eggertsson, G. H., Lavallée, Y., Kendrick, J. E. and Markússon, S.: Improving fluid flow in geothermal reservoirs by
thermal and mechanical stimulation: The case of Krafla volcano, Iceland, J. Volcanol. Geotherm. Res., submitted

Einstein, A.: A new determination of the molecular dimensions, Ann. Phys., 34, 591–592 (Translation of the 1906 German
720   version, 1911.

Elsworth, D. and Voight, B.: Evaluation of volcano flank instability triggered by dyke intrusion, Geol. Soc. London, Spec.
Publ., 110, 45–53, doi:10.1144/GSL.SP.1996.110.01.03, 1996.

Farquharson, J. I., Heap, M. J., Varley, N. R., Baud, P. and Reuschlé, T.: Permeability and porosity relationships of edifice-
forming andesites: A combined field and laboratory study, J. Volcanol. Geotherm. Res., 297, 52–68,
725   doi:10.1016/j.jvolgeores.2015.03.016, 2015.

Farquharson, J. I., Heap, M. J., Baud, P., Reuschlé, T. and Varley, N. R.: Pore pressure embrittlement in a volcanic edifice,
Bull. Volcanol., 78(1), 6, doi:10.1007/s00445-015-0997-9, 2016.

Fink, J. H. and Anderson, S. W.: Lava domes and coulees, in The Encyclopedia of Volcanoes, edited by H. Sigurdsson, B.
Houghton, H. Rymer, J. Stix, and S. McNutt, pp. 307–318, Academic Press., 2000.

730   Fluegel, A.: Glass viscosity calculation based on a global statistical modelling approach, Glas. Technol. J. Glas. …, 48(1),

13–30 [online] Available from: http://www.ingentaconnect.com/content/sgt/gt/2007/00000048/00000001/art00003, 2007.

Gent, A. N.: Theory of the parallel plate viscometer, Br. J. Appl. Phys., 11(February), 85–87, doi:10.1088/0508-3443/11/2/310, 1960.

Giordano, D., Russell, J. K. and Dingwell, D. B.: Viscosity of magmatic liquids: A model, Earth Planet. Sci. Lett., 271(1–4),
735 123–134, doi:10.1016/j.epsl.2008.03.038, 2008.

Gonnermann, H. M. and Manga, M.: The Fluid Mechanics Inside a Volcano, Annu. Rev. Fluid Mech., (39), 321–356, doi:10.1146/annurev.fluid.39.050905.110207, 2007.

Goto, A.: A new model for volcanic earthquake at Unzen Volcano: Melt rupture model, Geophys. Res. Lett., 26(16), 2541–2544, 1999.

740 Goto, Y., Nakada, S., Kurokawa, M., Shimano, T., Sugimoto, T., Sakuma, S., Hoshizumi, H., Yoshimoto, M. and Uto, K.: Character and origin of lithofacies in the conduit of Unzen volcano, Japan, J. Volcanol. Geotherm. Res., 175(1–2), 45–59, doi:10.1016/j.jvolgeores.2008.03.041, 2008.

Gottsmann, J., Lavallée, Y., Martí, J. and Aguirre-Díaz, G.: Magma-tectonic interaction and the eruption of silicic batholiths, Earth Planet. Sci. Lett., 284(3–4), 426–434, doi:10.1016/j.epsl.2009.05.008, 2009.

745 Griffiths, L., Heap, M. J., Xu, T., Chen, C. and Baud, P.: The influence of pore geometry and orientation on the strength and stiffness of porous rock, J. Struct. Geol., 96(February), 149–160, doi:10.1016/j.jsg.2017.02.006, 2017.

Hale, A. J. and Wadge, G.: The transition from endogenous to exogenous growth of lava domes with the development of shear bands, J. Volcanol. Geotherm. Res., 171, 237–257, doi:10.1016/j.jvolgeores.2007.12.016, 2008.

Harris, A. J. L., Flynn, L. P., Matías, O. and Rose, W. I.: The thermal stealth flows of Santiaguito dome , Guatemala :
750 Implications for the cooling and emplacement of dacitic block-lava flows, GSA Bull., (5), 533–546, 2002.

Heap, M. J. and Faulkner, D. R.: Quantifying the evolution of static elastic properties as crystalline rock approaches failure, Int. J. Rock Mech. Min. Sci., 45(4), 564–573, doi:10.1016/j.ijrmms.2007.07.018, 2008.

Heap, M. J., Vinciguerra, S. and Meredith, P. G.: The evolution of elastic moduli with increasing crack damage during cyclic stressing of a basalt from Mt. Etna volcano, Tectonophysics, 471(1–2), 153–160, doi:10.1016/j.tecto.2008.10.004, 2009.

755 Heap, M. J., Faulkner, D. R., Meredith, P. G. and Vinciguerra, S.: Elastic moduli evolution and accompanying stress changes with increasing crack damage: Implications for stress changes around fault zones and volcanoes during deformation, Geophys. J. Int., 183(1), 225–236, doi:10.1111/j.1365-246X.2010.04726.x, 2010.

Heap, M. J., Lavallée, Y., Laumann, A., Hess, K., Meredith, P. G. and Dingwell, D. B.: How tough is tuff in the event of fire?, Geology, 40(4), 311–314, doi:10.1130/G32940.1, 2012.

760 Heap, M. J., Lavallée, Y., Laumann, A., Hess, K., Meredith, P. G., Dingwell, D. B., Huismann, S. and Weise, F.: The influence of thermal-stressing (up to 1000 °C) on the physical , mechanical , and chemical properties of siliceous-aggregate , high-strength concrete, Constr. Build. Mater., 42, 248–265, doi:10.1016/j.conbuildmat.2013.01.020, 2013a.

Heap, M. J., Mollo, S., Vinciguerra, S., Lavallée, Y., Hess, K., Dingwell, D. B., Baud, P. and Iezzi, G.: Thermal weakening of the carbonate basement under Mt . Etna volcano (Italy): Implications for volcano instability, J. Volcanol. Geotherm.
765 Res., 250, 42–60, doi:10.1016/j.jvolgeores.2012.10.004, 2013b.

Heap, M. J., Lavallée, Y., Petrakova, L., Baud, P., Reuschlé, T., Varley, N. R. and Dingwell, D. B.: Microstructural controls on the physical and mechanical properties of edifice-forming andesites at Volcán de Colima, Mexico, J. Geophys. Res. Solid Earth, 119(4), 2925–2963, doi:10.1002/2013JB010521, 2014a.

Heap, M. J., Xu, T. and Chen, C.: The influence of porosity and vesicle size on the brittle strength of volcanic rocks and
770 magma, Bull. Volcanol., 76(9), 856, doi:10.1007/s00445-014-0856-0, 2014b.

Heap, M. J., Farquharson, J. I., Baud, P., Lavallée, Y. and Reuschlé, T.: Fracture and compaction of andesite in a volcanic edifice, Bull. Volcanol., 77(6), 55, doi:10.1007/s00445-015-0938-7, 2015a.

Heap, M. J., Farquharson, J. I. and Kolzenburg, S.: Timescales for permeability reduction and strength recovery in

densifying magma, Earth Planet. Sci. Lett., 429, 223–233, doi:http://dx.doi.org/10.1016/j.epsl.2015.07.053, 2015b.

775   Heap, M. J., Russell, J. K. and Kennedy, L. A.: Mechanical behaviour of dacite from Mount St . Helens (USA): A link between porosity and lava dome extrusion mechanism (dome or spine)?, J. Volcanol. Geotherm. Res., 328, 159–177, doi:10.1016/j.jvolgeores.2016.10.015, 2016a.

Heap, M. J., Wadsworth, F. B., Xu, T., Chen, C. and Tang, C.: The strength of heterogeneous volcanic rocks: A 2D approximation, J. Volcanol. Geotherm. Res., 319(April), 1–11, doi:10.1016/j.jvolgeores.2016.03.013, 2016b.

780   Hess, K., Cordonnier, B., Lavallée, Y. and Dingwell, D. B.: Viscous heating in rhyolite: An in situ experimental determination, Earth Planet. Sci. Lett., 275(1–2), 121–126, doi:10.1016/j.epsl.2008.08.014, 2008.

Hoek, E. and Bieniawski, Z. T.: Brittle Rock Fracture Propagation In Rock Under Compression Brittle Rock Fracture Propagation in Rock Under Compression, Int. J. Fract. Mech., 1(3), 137–155, doi:10.1007/BF00186851, 1965.

Hornby, A. J., Kendrick, J. E., Lamb, O. D., Hirose, T., De Angelis, S. H., Von Aulock, F. W., Umakoshi, K., Miwa, T.,
785   Henton De Angelis, S., Wadsworth, F. B., Hess, K., Dingwell, D. B. and Lavallée, Y.: Spine growth and seismogenic faulting at Mt. Unzen, Japan, J. Geophys. Res. Solid Earth, 120, doi:10.1002/2014JB011660, 2015.

IRSM Turkish National Group: Suggested methods for determining the uniaxial compressive strength and deformability of rock materials, Int. J. Rock Mech. Min. Sci. Geomech. Abstr., 16(2), 137–140, doi:10.1016/0148-9062(79)91450-5, 1979.

Kendrick, J. E., Lavallée, Y., Ferk, A., Perugini, D., Leonhardt, R. and Dingwell, D. B.: Extreme frictional processes in the
790   volcanic conduit of Mount St . Helens (USA) during the 2004-2008 eruption, J. Struct. Geol., 38, 61–76, doi:10.1016/j.jsg.2011.10.003, 2012.

Kendrick, J. E., Smith, R., Sammonds, P., Meredith, P. G., Dainty, M. and Pallister, J. S.: The influence of thermal and cyclic stressing on the strength of rocks from Mount St. Helens, Washington, Bull. Volcanol., 75(7), 1–12, doi:10.1007/s00445-013-0728-z, 2013a.

795   Kendrick, J. E., Lavallée, Y., Hess, K., Heap, M. J., Gaunt, H. E., Meredith, P. G. and Dingwell, D. B.: Tracking the permeable porous network during strain-dependent magmatic flow, J. Volcanol. Geotherm. Res., 260, 117–126, doi:10.1016/j.jvolgeores.2013.05.012, 2013b.

Kendrick, J. E., Lavallée, Y., Mariani, E., Dingwell, D. B., Wheeler, J. and Varley, N. R.: Crystal plasticity as an indicator of the viscous-brittle transition in magmas, Nat. Commun., 8(1), 1926, doi:10.1038/s41467-017-01931-4, 2017.

800   Kohashi, S., Shimokawa, S., Shimizu, K., Satohira, Y., Yamada, T. and Kimura, T.: Document for the committee of survey and countermeasure on lava dome collapse in Unzen Volcano (in Japanese)., 2012.

Kolzenburg, S., Heap, M. J., Lavallée, Y., Russell, J. K., Meredith, P. G. and Dingwell, D. B.: Strength and permeability recovery of tuffisite-bearing andesite, Solid Earth, 3(1), 191–198, doi:10.5194/se-3-191-2012, 2012.

Kueppers, U., Scheu, B., Spieler, O. and Dingwell, D. B.: Field-based density measurements as tool to identify preeruption
805   dome structure: set-up and first results from Unzen volcano, Japan, J. Volcanol. Geotherm. Res., 141(1–2), 65–75, doi:10.1016/j.jvolgeores.2004.09.005, 2005.

Kushnir, A. R. L., Martel, C., Bourdier, J.-L., Heap, M. J., Reuschlé, T., Erdmann, S., Komorowski, J.-C. and Cholik, N.: Probing permeability and microstructure: Unravelling the role of a low-permeability dome on the explosivity of Merapi (Indonesia), J. Volcanol. Geotherm. Res., 316, 56–71, doi:10.1016/j.jvolgeores.2016.02.012, 2016.

810   Lamb, O. D., De Angelis, S. H., Umakoshi, K., Hornby, A. J., Kendrick, J. E. and Lavallée, Y.: Repetitive fracturing during spine extrusion at Unzen volcano, Japan, Solid Earth, 6(4), 1277–1293, doi:10.5194/se-6-1277-2015, 2015.

Lamb, O. D., Angelis, S. De, Wall, R. J., Lamur, A., Varley, N. R., Reyes-Dávila, G., Arámbula-Mendoza, R., Hornby, A. J., Kendrick, J. E. and Lavallée, Y.: Seismic and experimental insights into eruption precursors at Volcán de Colima, Geophys. Res. Lett., doi:10.1002/2017GL073350, 2017.

815   Lamur, A., Kendrick, J. E., Eggertsson, G. H., Wall, R. J., Ashworth, J. D. and Lavallée, Y.: The permeability of fractured rocks in pressurised volcanic and geothermal systems, Sci. Rep., (May), 1–9, doi:10.1038/s41598-017-05460-4, 2017.

Laumonier, M., Arbaret, L., Burgisser, A. and Champallier, R.: Porosity redistribution enhanced by strain localization in crystal-rich magmas, Geology, 39(8), 715–718, doi:10.1130/G31803.1, 2011.

Lavallée, Y., Hess, K., Cordonnier, B. and Dingwell, D. B.: Non-Newtonian rheological law for highly crystalline dome lavas, Geology, 35(9), 843–846, doi:10.1130/G23594A.1, 2007.

Lavallée, Y., Meredith, P. G., Dingwell, D. B., Hess, K., Wassermann, J., Cordonnier, B., Gerik, A. and Kruhl, J. H.: Seismogenic lavas and explosive eruption forecasting., Nature, 453(7194), 507–510, doi:10.1038/nature06980, 2008.

Lavallée, Y., Varley, N. R., Alatorre-Ibargüengoitia, M. a., Hess, K., Kueppers, U., Mueller, S. P., Richard, D., Scheu, B., Spieler, O. and Dingwell, D. B.: Magmatic architecture of dome-building eruptions at Volcán de Colima, Mexico, Bull. Volcanol., 74(1), 249–260, doi:10.1007/s00445-011-0518-4, 2012.

Lavallée, Y., Heap, M. J., Kueppers, U., Kendrick, J. E. and Dingwell, D. B.: The fragility of Volcán de Colima – a material constraint, in Volcán de Colima – Managing the Threat, edited by N. R. Varley and J. C. Komorowski, Springer., 2018.

Lejeune, A. M. and Richet, P.: Rheology of crystal-bearing silicate melts : An experimental study at high viscosities, J. Geophys. Res., 100(B3), 4215–4229, 1995.

Lejeune, A. M., Bottinga, Y., Trull, T. W. and Richet, P.: Rheology of bubble-bearing magmas, Earth Planet. Sci. Lett., 166(1–2), 71–84, doi:http://dx.doi.org/10.1016/S0012-821X(98)00278-7, 1999.

Llewellin, E. W. and Manga, M.: Bubble suspension rheology and implications for conduit flow, J. Volcanol. Geotherm. Res., 143(1–3), 205–217, doi:10.1016/j.jvolgeores.2004.09.018, 2005.

Lopez, D. L. and Williams, S. N.: Catastrophic Volcanic Collapse: Relation to Hydrothermal Processes, Science (80-.)., 260(5115), 1794–1796, doi:10.1126/science.260.5115.1794, 1993.

Mader, H. M., Llewellin, E. W. and Mueller, S. P.: The rheology of two-phase magmas: A review and analysis, J. Volcanol. Geotherm. Res., 257, 135–158, doi:10.1016/j.jvolgeores.2013.02.014, 2013.

Manga, M., Castro, J. M., Cashman, K. V. and Lowewenberg, M.: Rheology of bubble-bearing magmas, J. Volcanol. Geotherm. Res., 87, 15–28, 1998.

Martel, C. and Schmidt, B. C.: Decompression experiments as an insight into ascent rates of silicic magmas, Contrib. to Mineral. Petrol., 397–415, doi:10.1007/s00410-002-0404-3, 2003.

Matsushima, T. and Takagi, A.: GPS and EDM monitoring of Unzen Volcano ground deformation, Earth, Planets Sp., 52(11), 1015–1018 [online] Available from: http://svr4.terrapub.co.jp/journals/EPS/pdf/5211/52111015.pdf (Accessed 5 November 2013), 2000.

Maxwell, J. C.: On the dynamical theory of gases, Phil Trans. Roy. Soc. Lond., 157, 49–88, doi:10.1098/rstl.1867.0004, 1867.

McKenzie, D. and Holness, M.: Local deformation in compacting flows: Development of pressure shadows, Earth Planet. Sci. Lett., 180(1–2), 169–184, doi:10.1016/S0012-821X(00)00152-7, 2000.

Mueller, S., Melnik, O., Spieler, O., Scheu, B. and Dingwell, D. B.: Permeability and degassing of dome lavas undergoing rapid decompression: An experimental determination, Bull. Volcanol., 67(6), 526–538, doi:10.1007/s00445-004-0392-4, 2005.

Mueller, S., Scheu, B., Kueppers, U., Spieler, O., Richard, D. and Dingwell, D. B.: The porosity of pyroclasts as an indicator of volcanic explosivity, J. Volcanol. Geotherm. Res., 203(3–4), 168–174, doi:10.1016/j.jvolgeores.2011.04.006, 2011a.

Mueller, S. P., Llewellin, E. W. and Mader, H. M.: The effect of particle shape on suspension viscosity and implications for magmatic flows, Geophys. Res. Lett., 38(13), 1–5, doi:10.1029/2011GL047167, 2011b.

Nakada, S. and Fujii, T.: Preliminary report on the activity at Unzen Volcano (Japan), November 1990-November 1991: Dacite lava domes and pyroclastic flows, J. Volcanol. Geotherm. Res., 54(3–4), 319–333, doi:10.1016/0377-0273(93)90070-8, 1993.

Nakada, S. and Motomura, Y.: Petrology of the 1991-1995 eruption at Unzen: Effusion pulsation and groundmass

860   crystallization, J. Volcanol. Geotherm. Res., 89(1–4), 173–196, doi:10.1016/S0377-0273(98)00131-0, 1999.

Nakada, S., Miyake, Y., Sato, H., Oshima, O. and Fujinawa, A.: Endogenous growth of dacite dome at Unzen volcano (Japan), 1993-1994, Geology, 23(2), 157, doi:10.1130/0091-7613(1995)023<0157:EGODDA>2.3.CO;2, 1995a.

Nakada, S., Miyake, Y., Sato, H., Oshima, O. and Fujinawa, A.: Endogenous growth of dacite dome at Unzen volcano (Japan), 1993–1994, Geology, 23(2), 157, doi:10.1130/0091-7613(1995)023<0157:EGODDA>2.3.CO;2, 1995b.

865   Nakada, S., Shimizu, H. and Ohta, K.: Overview of the 1990 – 1995 eruption at Unzen Volcano, J. Volcanol. Geotherm. Res., (89), 1–22, doi:10.1016/S0377-0273(98)00118-8, 1999a.

Nakada, S., Shimizu, H. and Ohta, K.: Overview of the 1990 – 1995 eruption at Unzen Volcano, J. Volcanol. Geotherm. Res., 89(89), 1–22, doi:10.1016/S0377-0273(98)00118-8, 1999b.

NASA/METI/AIST/Japan Spacesystems, and U. S. /Japa. A. S. T.: NASA EOSDIS Land Processes DAAC ASTER, DEM
870   Prod. N032E130, doi:10.5067/ASTER/AST14DEM.003, 2001.

Ostwald, W.: Concerning the function rate of the viscosity of dispersion systems, , 36(4), 248–250, 1925.

Pallister, B. J. S., Thornber, C. R., Cashman, K. V., Clynne, M. a, Lowers, H. a, Mandeville, C. W., Brownfield, I. K. and Meeker, G. P.: Petrology of the 2004 – 2006 Mount St . Helens Lava Dome — Implications for Magmatic Plumbing and Eruption Triggering, in A Volcano Rekindled: The Renewed Eruption of Mount St. Helens 2004-2006, U.S. Geological
875   Survey Professional Paper 1750, edited by D. R. Sherrod, W. E. Scott, and P. H. Stauffer, pp. 647–702., 2008.

Paterson, M. S. and Wong, T.: Experimental Rock Deformation: The Brittle Field, 2nd Edition, Second Edi., Springer, Berlin Heidelberg., 2005.

Pierson, T. C., Janda, R. J., Thouret, J.-C. and Borrero, C. A.: Perturbation and melting of snow and ice by the 13 November 1985 eruption of Nevado del Ruiz , Colombia , and consequent mobilization , flow and deposition of lahars, J. Volcanol.
880   Geotherm. Res., 41, 17–66, 1990.

Pola, A., Crosta, G., Fusi, N., Barberini, V. and Norini, G.: Influence of alteration on physical properties of volcanic rocks, Tectonophysics, 566–567, 67–86, doi:10.1016/j.tecto.2012.07.017, 2012.

Quane, S. L. and Russell, J. K.: Welding: insights from high-temperature analogue experiments, J. Volcanol. Geotherm. Res., 142(1–2), 67–87, doi:10.1016/j.jvolgeores.2004.10.014, 2005.

885   Reid, M. E., Keith, T. E. C., Kayen, R. E., Iverson, N. R., Iverson, R. M. and Brien, D. L.: Volcano collapse promoted by progressive strength reduction: New data from Mount St. Helens, Bull. Volcanol., 72(6), 761–766, doi:10.1007/s00445-010-0377-4, 2010.

Reiner, M.: The Deborah Number, Phys. Today, 17(1), 62, doi:10.1063/1.3051374, 1964.

Roscoe, R.: The viscosity of suspensions of rigid spheres, Br. J. Appl. Phys., 3(8), 267–269, doi:10.1088/0508-3443/3/8/306,
890   1952.

Rust, A. C. and Manga, M.: Effects of bubble deformation on the viscosity of dilute suspensions, J. Non-Newtonain Fluid Mechanaics, 104, 53–63, 2002.

Sakuma, S., Kajiwara, T., Nakada, S., Uto, K. and Shimizu, H.: Drilling and logging results of USDP-4 - Penetration into the volcanic conduit of Unzen Volcano, Japan, J. Volcanol. Geotherm. Res., 175(1–2), 1–12,
895   doi:10.1016/j.jvolgeores.2008.03.039, 2008.

Sammis, C. G. and Ashby, M. F.: The failure of brittle porous solids under compressive stress states, Acta Metall., 34(3), 511–526, 1986.

Schaefer, L. N., Kendrick, J. E., Oommen, T., Lavallée, Y. and Chigna, G.: Geomechanical rock properties of a basaltic volcano, Front. Earth Sci., 3(June), 1–15, doi:10.3389/feart.2015.00029, 2015.

900   Scholz, C. H.: Microfracturing and the inelastic deformation of rock in compression, J. Geophys. Res., 73(4), 1417, doi:10.1029/JB073i004p01417, 1968.

Scott, W. E., Sherrod, D. R. and Gardner, C. A.: Overview of the 2004 to 2006, and continuing, eruption of Mount St.

Helens, Washington, in A Volcano Rekindled: The Renewed Eruption of Mount St. Helens, 2004-2006, U.S. Geological Survey Professional Paper 1750, vol. 1750, edited by D. R. Sherrod, W. E. Scott, and P. H. Stauffer, pp. 3–22. [online]
905 Available from: http://pubs.usgs.gov/pp/1750/chapters/pp2008-1750_chapter01.pdf, 2008.

Siebert, L., Glicken, H. and Ui, T.: Volcanic hazards from Bezymianny- and Bandai-type eruptions, Bull. Volcanol., 49(1), 435–459, doi:10.1007/BF01046635, 1987.

Siebert, L., Cottrell, E., Venzke, E. and Andrews, B.: Earth's Volcanoes and Their Eruptions: An Overview, in The Encyclopedia of Volcanoes, edited by H. Sigurdsson, B. F. Houghton, S. McNutt, H. Rymer, and J. Stix, pp. 239–256,
910 Elsevier., 2015.

de Silva, S. and Lindsay, J. M.: Primary Volcanic Landforms, in The Encyclopedia of Volcanoes, edited by H. Sigurdsson, B. Houghton, S. McNutt, H. Rymer, and J. Stix, pp. 273–298, Elsevier., 2015.

Smith, R., Kilburn, C. R. J. and Sammonds, P. R.: Rock fracture as a precursor to lava dome eruptions at Mount St Helens from June 1980 to October 1986, Bull. Volcanol., 69(6), 681–693, doi:10.1007/s00445-006-0102-5, 2007.

915 Smith, R., Sammonds, P. R., Tuffen, H. and Meredith, P. G.: Evolution of the mechanics of the 2004-2008 Mt. St. Helens lava dome with time and temperature, Earth Planet. Sci. Lett., 307(1–2), 191–200, doi:10.1016/j.epsl.2011.04.044, 2011.

Sparks, R. S. J. and Young, S. R.: The eruption of Soufrière Hills Volcano , Montserrat (1995-1999): overview of scientific results, in The Eruption of Soufri~re Hills Volcano, Montserrat, from 1995 to 1999., edited by T. H. Druitt and B. P. Kokelaar, pp. 45–69, Geological Society, London, Memoirs., 2002.

920 Stasiuk, M. V. and Jaupart, C.: Lava flow shapes and dimensions as reflections of magma system conditions, J. Volcanol. Geotherm. Res., 78(1–2), 31–50, doi:10.1016/S0377-0273(97)00002-4, 1997.

Surono, Jousset, P., Pallister, J., Boichu, M., Buongiorno, M. F., Budisantoso, A., Costa, F., Andreastuti, S., Prata, F., Schneider, D., Clarisse, L., Humaida, H., Sumarti, S., Bignami, C., Griswold, J., Carn, S., Oppenheimer, C. and Lavigne, F.: The 2010 explosive eruption of Java's Merapi volcano-A "100-year" event, J. Volcanol. Geotherm. Res., 241–242, 121–135,
925 doi:10.1016/j.jvolgeores.2012.06.018, 2012.

Takarada, S., Miyabuchi, Y., Hoshizumi, H., Matsushima, T. and Nagai, D.: A02: Unzen and Aso volcanoes, central Kyushu, Japan: Unzen's new lava dome climb and 1991-95 poyroclastic flows and Aso's active crater and one of the largest calderas in Japan, 2013.

Tanguy, J. C.: Rapid dome growth at Montagne Pelée during the early stages of the 1902-1905 eruption: A reconstruction
930 from Lacroix's data, Bull. Volcanol., 66(7), 615–621, doi:10.1007/s00445-004-0344-z, 2004.

Truby, J. M., Mueller, S. P., Llewellin, E. W. and Mader, H. M.: The rheology of three-phase suspensions at low bubble capillary number., Proc. Math. Phys. Eng. Sci., 471(2173), 20140557, doi:10.1098/rspa.2014.0557, 2015.

Umakoshi, K., Takamura, N., Shinzato, N., Uchida, K., Matsuwo, N. and Shimizu, H.: Seismicity associated with the 1991–1995 dome growth at Unzen Volcano, Japan, J. Volcanol. Geotherm. Res., 175(1–2), 91–99,
935 doi:10.1016/j.jvolgeores.2008.03.030, 2008.

Vallance, J. W., Schneider, D. J. and Schilling, S. P.: Growth of the 2004-2006 Lava-Dome Complex at Mount St. Helens, Washington, in A Volcano Rekindled: The Renewed Eruption of Mount St. Helens 2004-2006, edited by D. R. Sherrod, W. E. Scott, and P. H. Stauffer, pp. 169–208, U.S. Geological Survey Professional Paper 1750., 2008.

Venezky, D. Y. and Rutherford, M. J.: Petrology and Fe–Ti oxide reequilibration of the 1991 Mount Unzen mixed magma, J.
940 Volcanol. Geotherm. Res., 89(1–4), 213–230, doi:10.1016/S0377-0273(98)00133-4, 1999.

Voight, B.: Structural stability of andesite volcanoes and lava domes, Philos. Trans. R. Soc. London, 358, 1663–1703, doi:10.1098/rsta.2000.0609, 2000.

Voight, B. and Elsworth, D.: Failure of volcano slopes, Geotechnique, 47(1), 1–31, 1997.

Voight, B. and Elsworth, D.: Instability and collapse of hazardous gas-pressurized lava domes, Geophys. Res. Lett., 27(1),
945 1–4, 2000.

Voight, B., Glicken, H., Janda, J. and Douglass, P. M.: Catastrophic rockslide avalanche of May 18, in The 1980 eruptions of Mount St Helens, Washington, vol. 1250, edited by P. W. Lipman and D. R. Mullineaux, pp. 347–378, Geological Survey Professional Paper., 1981.

950   Voight, B., Sparks, R. S. J., Miller, A. D., Stewart, R. C., Hoblitt, R. P., Clarke, A., Ewart, J., Aspinall, W. P., Baptie, B., Calder, E. S., Cole, P. D., Druitt, T. H., Hartford, C., Herd, R. A., Jackson, P., Lejeune, A. M., Lockhart, A. B., Loughlin, S. C., Luckett, R., Lynch, L., Norton, G. E., Robertson, R., Watson, I. M., Watts, R. and Young, S. R.: Magma Flow Instability and Cyclic Activity at Soufriere Hills Volcano , Montserrat , British West Indies, , 643(May), 2009.

Vona, A., Romano, C., Dingwell, D. B. and Giordano, D.: The rheology of crystal-bearing basaltic magmas from Stromboli and Etna, Geochim. Cosmochim. Acta, 75(11), 3214–3236, doi:10.1016/j.gca.2011.03.031, 2011.

955   Vona, A., Romano, C., Giordano, D. and Russell, J. K.: The multiphase rheology of magmas from Monte Nuovo (Campi Flegrei, Italy), Chem. Geol., 346, 213–227, doi:10.1016/j.chemgeo.2012.10.005, 2013.

Wadsworth, F. B., Witcher, T., Vasseur, J., Dingwell, D. B. and Scheu, B.: When Does Magma Break?, in Advances in Volcanology, Springer, Berlin, Heidelberg., 2017.

Wallace, P. A., Kendrick, J. E., Ashworth, J. D., Miwa, T., Coats, R., De Angelis, S. H., Mariani, E., Utley, J., Biggan, A.
960   and Lavallée, Y.: Petrological architecture of a magmatic shear zone: A multidisciplinary investigation of strain localisation during magma ascent at Unzen volcano, Japan, submitted

Walter, T. R., Troll, V. R., Cailleau, B., Belousov, A., Schmincke, H. U., Amelung, F. and Bogaard, P.: Rift zone reorganization through flank instability in ocean island volcanoes: An example from Tenerife, Canary Islands, Bull. Volcanol., 67(4), 281–291, doi:10.1007/s00445-004-0352-z, 2005.

965   Webb, S. L. and Dingwell, D. B.: The onset of non-Newtonian rheology of silicate melts - A fiber elongation study, Phys. Chem. Miner., 17(2), 125–132, doi:10.1007/BF00199663, 1990.

Webb, S. L. and Knoche, R.: The glass-transition, structural relaxation and shear viscosity of silicate melts, Chem. Geol., 128(1–4), 165–183, doi:10.1016/0009-2541(95)00171-9, 1996.

Yamamoto, T., Takarada, S. and Suto, S.: Pyroclastic flows from the 1991 eruption of Unzen volcano, Japan, Bull.
970   Volcanol., 55(3), 166–175, doi:10.1007/BF00301514, 1993.

Yilmaz, T. I., Gilg, H. ., Wallace, P. A., Hess, K. U., Wadsworth, F. B., Utley, J., Kendrick, J. E., Lavallée, Y., Nakada, S. and Dingwell, D. B.: Rapid three-stage clay alteration of conduit dykes from the Mt Unzen USDP-4 drill core, Geology, submitted

Young, S. R., Sparks, R. S. J., Aspinall, W. P., Lynch, L. L., Miller, A. D., Robertson, R. E. A. and Shepherd, J. B.:
975   Overview of the eruption of Soufriere Hills Volcano, Montserrat, 18 July 1995 to December 1997, Geophys. Res. Lett., 25(18), 3389–3392, doi:10.1029/98GL01405, 1998.
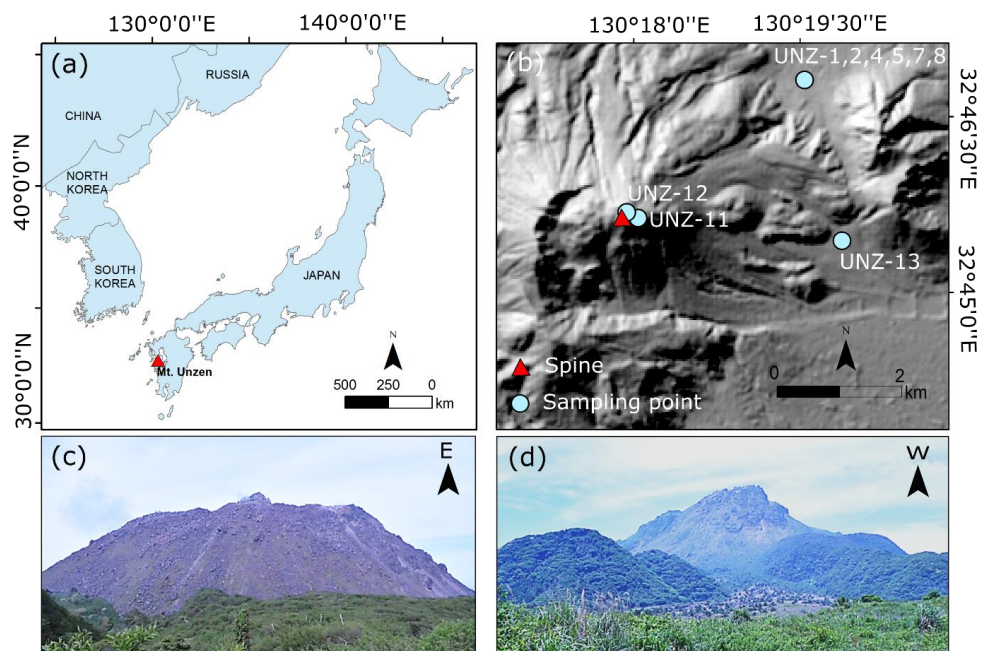
Figure 1. (a) Location of Mt. Unzen in South Western Japan; (b) Sample collection locations and location of the erupted spine, the summit of Mt. Unzen at 1500 m above sea level (NASA/METI/AIST/Japan Spacesystems, 2001); view of Mt. Unzen lava dome looking East ~ 0.62 km from the spine (c) and West ~ 3.87 km from the spine (d) in 2016.
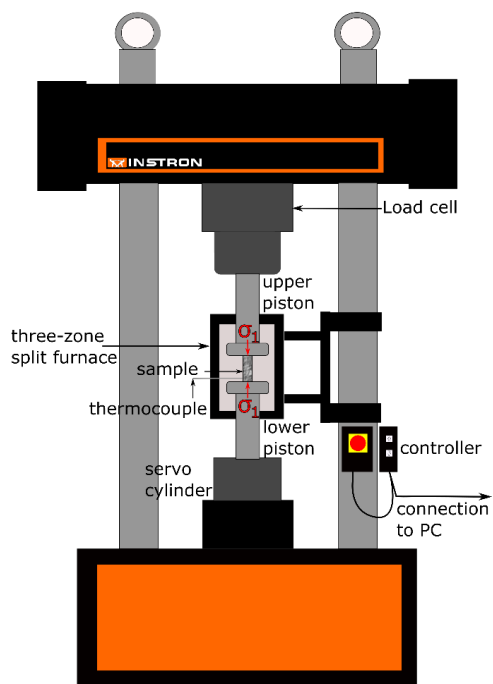
985   **Figure 2. Schematic of the uniaxial compressive strength testing set-up in the Experimental Volcanology and Geothermal Research Laboratory at the University of Liverpool. An 100 kN Instron 8862 uniaxial press with a three-zone, split cylinder furnace was used to perform experiments at varying strain rates and temperatures.**
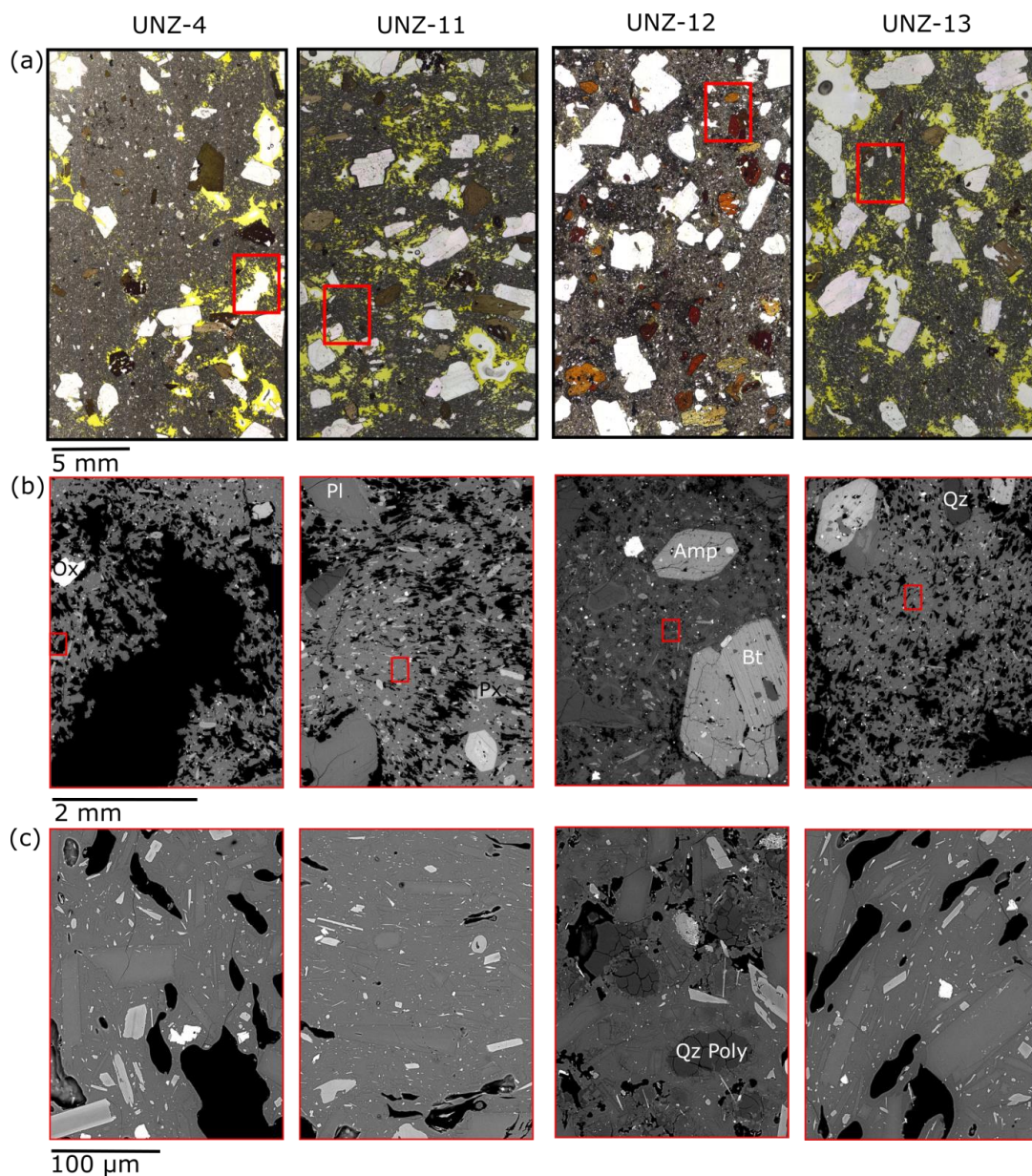
Figure 3. Plane–polarised light (a) and backscattered electron images (b,c) of undeformed samples UNZ-4,-11, -12 and -13. (b) is a zoom into the red box in (a), and (c) is a zoom in of the red box in (b), displaying the groundmass textures. Amp: Amphibole, Bt: Biotite, Ox: Oxides, Pl: Plagioclaise, Px: Pyroxene, Qz, Quartz, Qz Poly: Quartz Polymorph. Images are orientated so that the later applied principal stress, σ1, is in the vertical direction. [Note the scale that is below each set of images.]
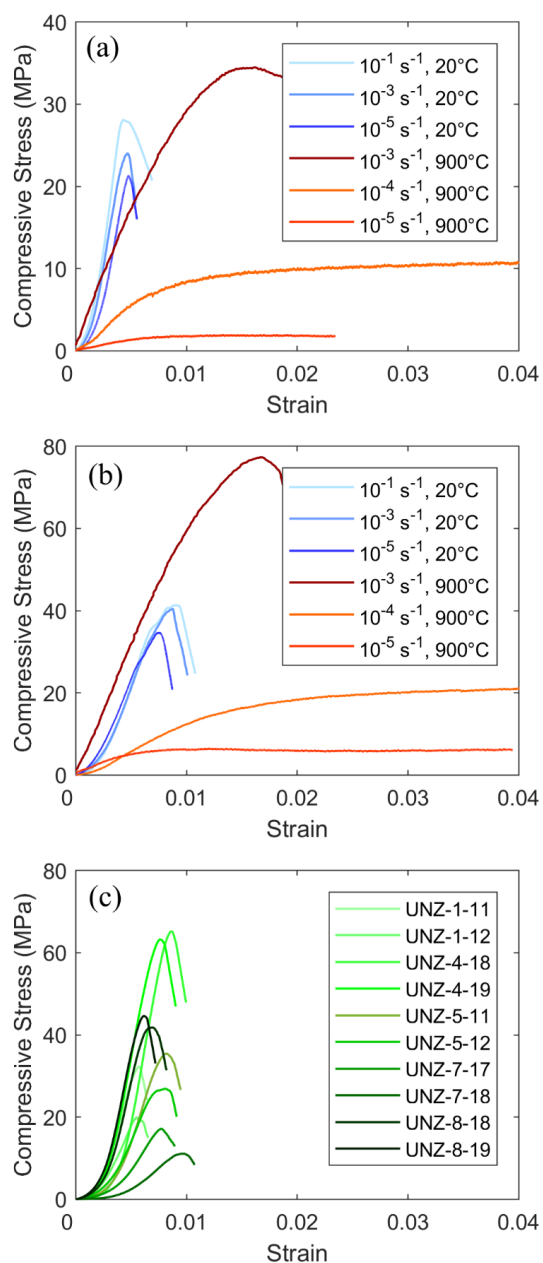
Figure 4. Examples of compressive stress-strain curves for (a) high porosity, UNZ-1 (0.21); (b) low porosity, UNZ-4 (0.12) at a range of rates and temperatures and (c) thermally stressed samples, all performed at a strain rate of 10^{-3} s^{-1}. Mechanical data for high temperature experiments are shown in shades of red, low temperature experiments in shades of blue and thermally stressed experiments in shades of green. At high temperature, faster strain rates cause the sample to break whereas at slower strain rates the sample flows. Brittle high temperature experiments fail at considerably higher peak stresses than those performed at ambient temperatures. In the brittle regime, samples deformed at faster rates failed at higher stresses. [Note: there is a difference in Y-scale between (a) and (b) & (c)]

1000

1005
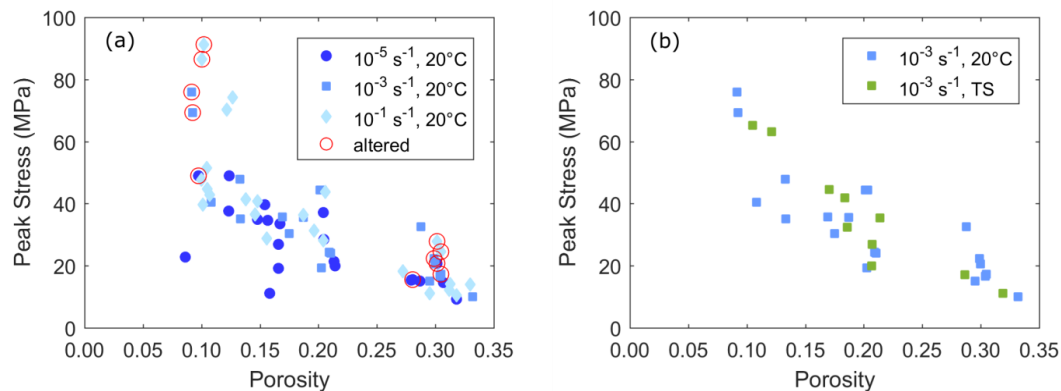
Figure 5. (a) The strength (peak stress) of samples tested at ambient temperatures at varying strain rates, highlighting the apparent strengthening of materials deformed at faster rate. Red rings circle the samples that are visibly altered. (b) A comparison of samples that were thermally stressed and those that were not, both tested at ambient temperatures and strain rates of 10^{-3} s^{-1},

1010   **demonstrating that there is no change in strength as a function of porosity due to thermal stressing.**
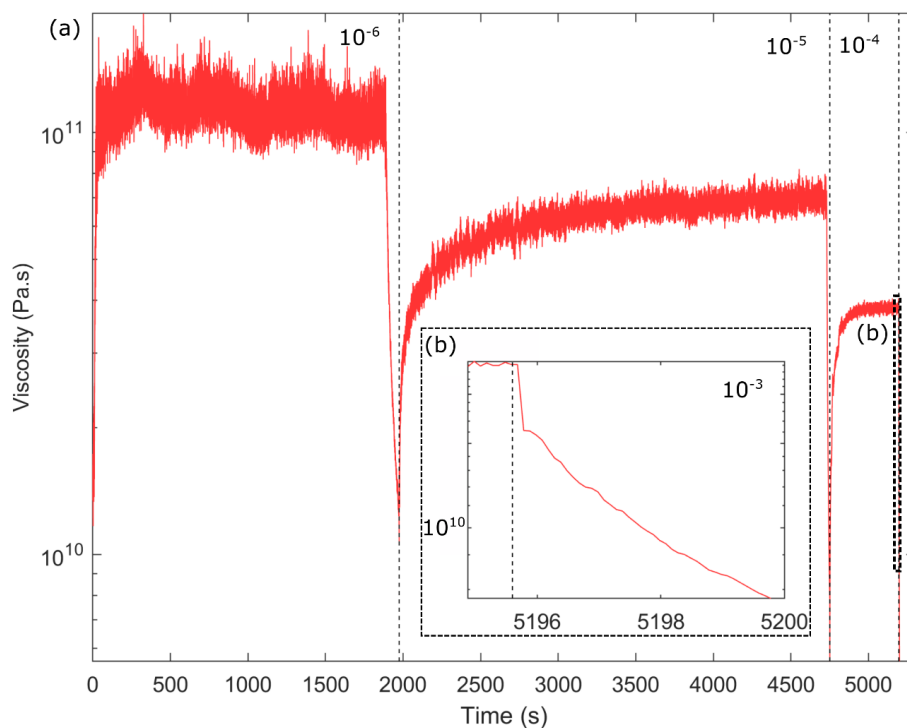
Figure 6. Apparent viscosity evolution of UNZ-1 (porosity: 0.22) at 900 ˚C during a stepped strain-rate experiment (10^{-6} s^{-1}, 10^{-5} s^{-1}, 10^{-4} s^{-1}, 10^{-3} s^{-1}); each step is separated by dashed lines. The insert zooms in on the apparent viscosity decrease that accompanies sample failure at 10^{-3} s^{-1}. The decrease in viscosity at each increasing strain rate increment highlights the shear thinning behaviour of these lavas.

1015
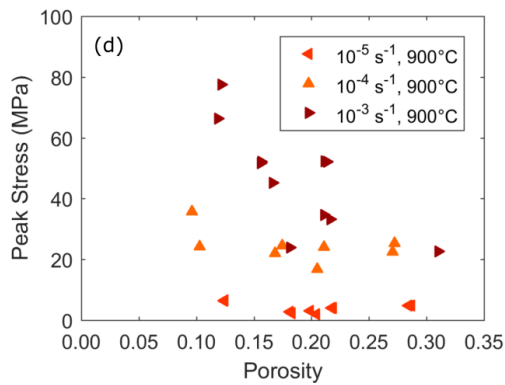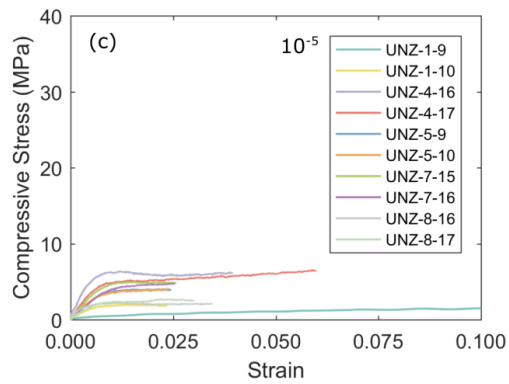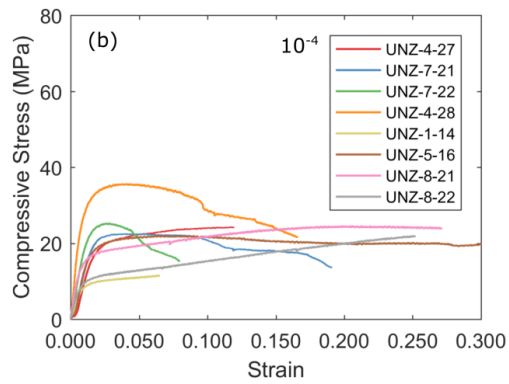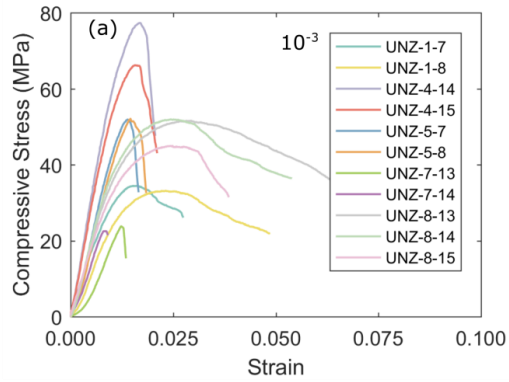
1020 **Figure 7. High temperature uniaxial experiment results, including stress-strain curves for samples tested at a strain rates of (a) 1^{0-3} s^{-1}, (b) 10^{-4} s^{-1}, and (c) 10^{-5} s^{-1}, demonstrating the shift from viscous flow at low rate to increasingly brittle deformation at faster rate. (d) The peak stresses achieved during each experiment carried out at 900 ˚C further highlights this observation and shows the porosity-dependence of strength in the brittle regime.**
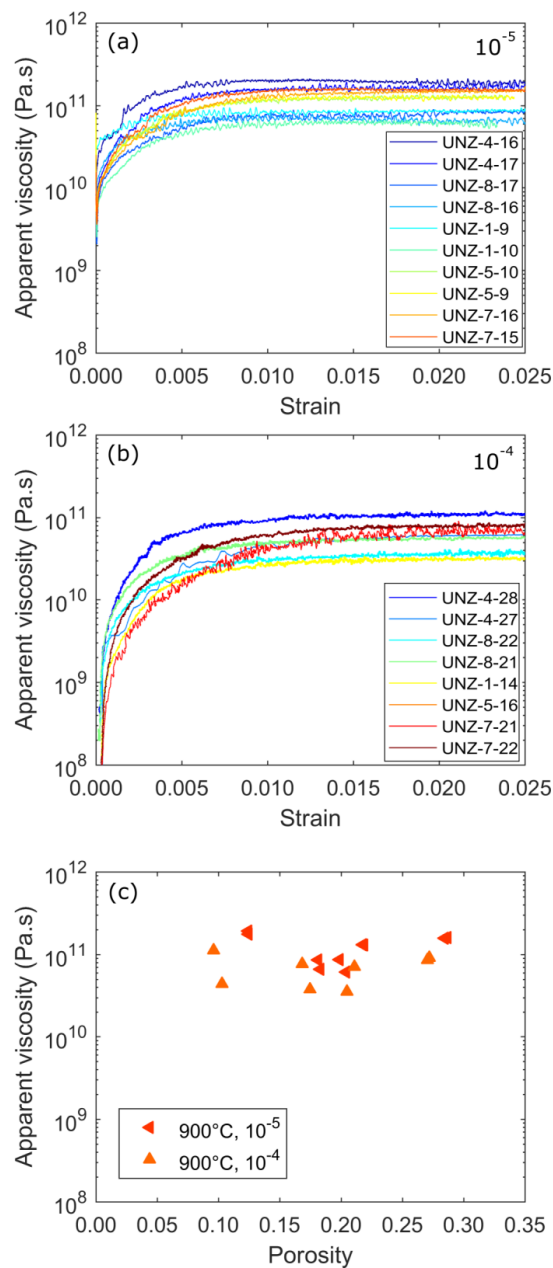
1025 **Figure 8. Apparent viscosities of porous lavas at 900 ˚C for strain rates of (a) 10^{-5} s^{-1} and (b) 10^{-4} s^{-1}; colours warm from blue to red with increasing sample porosity. (c) Compilation of apparent viscosities as a function of porosity for samples tested at strain rates of 10^{-4} s^{-1} and 10^{-5} s^{-1}. Viscosities decrease between strain rates of 10^{-5} to 10^{-4} s^{-1}, an example of shear thinning in the Unzen samples. Porosity has no control on the apparent viscosities of the samples tested here.**
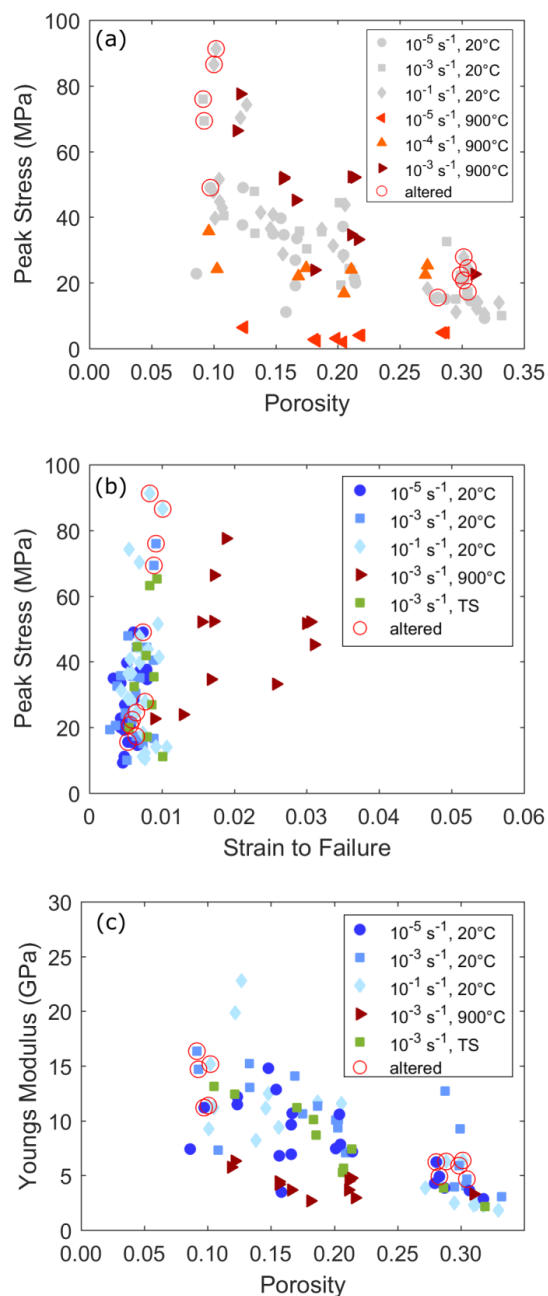
1030

Figure 9. Strength and Young's Moduli of Unzen rocks and lavas at different conditions. Shades of blue represent tests carried out at ambient temperatures, shades of red indicate those performed at 900 °C, and shades of green depict thermally stressed samples which were tested in ambient conditions. The red rings circle the samples which were deemed visibly altered at collection. (a) Peak stress with porosity for all completed experiments. Low temperature tests, as seen in Figure 5 (b), are faded to grey. (b) Peak stress with strain at the point of sample failure (i.e. the stain at peak stress) for all experiments with a brittle response. (c) Young's modulus as a function of porosity for all samples that had a brittle response, calculated using the slope of the linear portion of the stress-strain curve (see Fig. S6).

1035
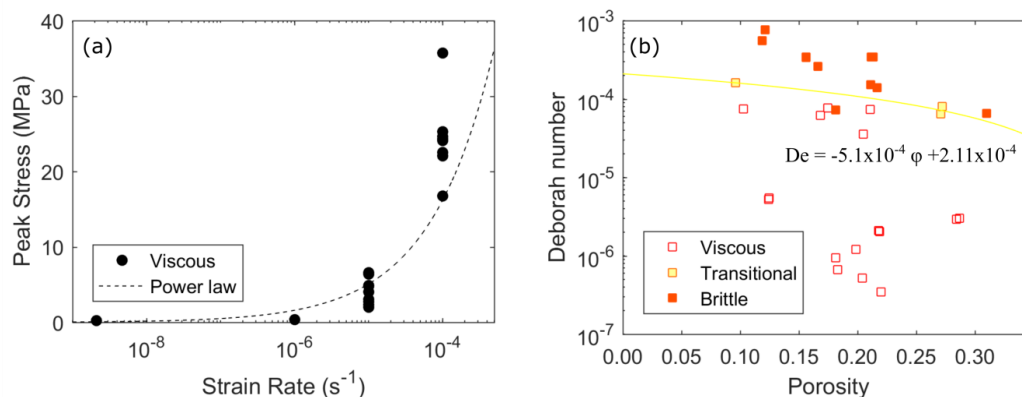
Figure 10. (a) Peak stress plotted with strain rate for completed experiments, in semi-log space. The power law equation of the line
1040 **is shown on the figure. Oswald constants k and b are 1606 and 0.7755 respectively. (b) The calculated Deborah number as a function of porosity for each sample tested at high temperature, in semi-log space. Depending on the shape of the stress-strain curve for each sample, it was labelled as viscous, transitional or brittle. The critical Deborah number, De_c, which marks the onset of brittle deformation is approximately 2.11×10^{-4}**

Sample	Total porosity	Connected porosity	Strain rate (s^{-1})	Temperature (°C)	Peak force (N)	Peak Stress (MPa)	Strain to failure	Thermally treated	Altered	Viscosity (Pa.s)	De number	Young's modulus (GPa)
UNZ-1-2	0.21	0.19	1.E-05	20	6789	21.38	0.0049	N	N	N/A	N/A	7.45
UNZ-4-13	0.09	0.07	1.E-05	20	7180	22.71	0.0043	N	N	N/A	N/A	7.40
UNZ-5-1	0.20	0.18	1.E-05	20	11779	37.09	0.0070	N	N	N/A	N/A	10.58
UNZ-5-5	0.20	0.19	1.E-05	20	9022	28.49	0.0061	N	N	N/A	N/A	7.84
UNZ-7-1	0.29	0.28	1.E-05	20	4750	15.10	0.0071	N	N	N/A	N/A	3.85
UNZ-7-10	0.31	0.30	1.E-05	20	4600	14.63	0.0066	N	N	N/A	N/A	3.63
UNZ-7-12	0.32	0.31	1.E-05	20	2895	9.20	0.0046	N	N	N/A	N/A	2.86
UNZ-7-6	0.28	0.28	1.E-05	20	4889	15.41	0.0060	N	N	N/A	N/A	4.27
UNZ-8-1	0.17	0.17	1.E-05	20	6000	19.15	0.0048	N	N	N/A	N/A	6.93
UNZ-8-10	0.15	0.15	1.E-05	20	12570	39.62	0.0052	N	N	N/A	N/A	12.84
UNZ-8-12	0.17	0.14	1.E-05	20	10600	33.44	0.0043	N	N	N/A	N/A	10.67
UNZ-8-6	0.17	0.17	1.E-05	20	8540	26.90	0.0049	N	N	N/A	N/A	9.65
UNZ-4-25	0.16	0.14	1.E-05	20	3497	11.07	0.0048	N	N	N/A	N/A	3.48
UNZ-4-26	0.16	0.11	1.E-05	20	10981	34.64	0.0080	N	N	N/A	N/A	6.79
UNZ-1-0	0.21	0.19	1.E-05	20	6320	19.92	0.0043	N	N	N/A	N/A	7.16
UNZ-2-4	0.12	0.10	1.E-05	20	13361	41.98	0.0061	N	N	N/A	N/A	12.19
UNZ-2-5	0.12	0.10	1.E-05	20	11957	37.68	0.0079	N	N	N/A	N/A	11.50
UNZ-12-4	0.10	0.09	1.E-05	20	15549	48.95	0.0074	N	Y	N/A	N/A	11.18
UNZ-11-2	0.30	0.28	1.E-05	20	6592	20.71	0.0056	N	Y	N/A	N/A	6.21
UNZ-11-3	0.28	0.27	1.E-05	20	4950	15.60	0.0053	N	Y	N/A	N/A	4.88
UNZ-8-21	0.15	0.12	1.E-05	20	11073	34.90	0.0033	N	N	N/A	N/A	14.77
UNZ-1-4	0.21	0.18	1.E-03	20	7681	24.42	0.0050	N	N	N/A	N/A	7.06
UNZ-1-6	0.21	0.18	1.E-03	20	7639	24.08	0.0050	N	N	N/A	N/A	7.19
UNZ-5-2	0.20	0.18	1.E-03	20	14081	44.47	0.0079	N	N	N/A	N/A	10.04
UNZ-5-3	0.20	0.19	1.E-03	20	14065	44.33	0.0065	N	N	N/A	N/A	10.11
UNZ-7-11	0.33	0.33	1.E-03	20	3150	9.98	0.0052	N	N	N/A	N/A	3.05

UNZ-7-2	0.30	0.29	1.E-03	20	5250	16.70	0.0089	N	N	N/A	N/A	4.05
UNZ-7-7	0.30	0.29	1.E-03	20	4750	15.01	0.0074	N	N	N/A	N/A	3.97
UNZ-8-11	0.19	0.17	1.E-03	20	11300	35.53	0.0059	N	N	N/A	N/A	11.32
UNZ-8-3	0.18	0.15	1.E-03	20	9640	30.39	0.0064	N	N	N/A	N/A	10.63
UNZ-8-7	0.17	0.14	1.E-03	20	11350	35.73	0.0043	N	N	N/A	N/A	14.08
UNZ-4-24	0.11	0.09	1.E-03	20	12841	40.47	0.0088	N	N	N/A	N/A	7.30
UNZ-2-1	0.13	0.11	1.E-03	20	15241	47.94	0.0053	N	N	N/A	N/A	15.22
UNZ-2-6	0.13	0.11	1.E-03	20	11115	35.13	0.0070	N	N	N/A	N/A	13.04
UNZ-13-1	0.29	0.27	1.E-03	20	10341	32.52	0.0038	N	N	N/A	N/A	12.70
UNZ-13-2	0.30	0.29	1.E-03	20	6544	20.58	0.0036	N	N	N/A	N/A	9.25
UNZ-12-1	0.09	0.09	1.E-03	20	22126	69.32	0.0089	N	Y	N/A	N/A	14.71
UNZ-12-3	0.09	0.10	1.E-03	20	24227	75.97	0.0092	N	Y	N/A	N/A	16.33
UNZ-11-4	0.30	0.30	1.E-03	20	7066	22.25	0.0059	N	Y	N/A	N/A	5.90
UNZ-11-6	0.30	0.30	1.E-03	20	5507	17.32	0.0065	N	Y	N/A	N/A	4.65
UNZ-1-14	0.20	0.18	1.E-03	20	7681	19.25	0.0028	N	N	N/A	N/A	9.34
UNZ-1-11	0.19	0.16	1.E-03	20	10257	32.36	0.0062	Y	N	N/A	N/A	8.69
UNZ-1-12	0.21	0.18	1.E-03	20	6334	19.92	0.0055	Y	N	N/A	N/A	5.26
UNZ-4-18	0.10	0.09	1.E-03	20	20556	65.17	0.0093	Y	N	N/A	N/A	13.11
UNZ-4-19	0.12	0.10	1.E-03	20	19939	63.22	0.0083	Y	N	N/A	N/A	12.40
UNZ-5-11	0.21	0.21	1.E-03	20	11240	35.42	0.0089	Y	N	N/A	N/A	7.39
UNZ-5-12	0.21	0.21	1.E-03	20	8515	26.89	0.0086	Y	N	N/A	N/A	5.64
UNZ-7-17	0.29	0.29	1.E-03	20	5412	17.16	0.0080	Y	N	N/A	N/A	3.87
UNZ-7-18	0.32	0.32	1.E-03	20	3515	11.10	0.0101	Y	N	N/A	N/A	2.14
UNZ-8-18	0.18	0.16	1.E-03	20	13266	41.81	0.0078	Y	N	N/A	N/A	10.10
UNZ-8-19	0.17	0.15	1.E-03	20	14175	44.63	0.0066	Y	N	N/A	N/A	11.19
UNZ-1-1	0.20	0.17	1.E-01	20	9970	31.33	0.0044	N	N	N/A	N/A	9.83
UNZ-1-3	0.20	0.18	1.E-01	20	8936	28.11	0.0058	N	N	N/A	N/A	8.66
UNZ-4-20	0.10	0.09	1.E-01	20	16342	51.55	0.0095	N	N	N/A	N/A	8.51

UNZ-4-22	0.14	0.09	1.E-01	20	13050	41.33	0.0096	N	N	N/A	N/A	8.20
UNZ-4-4	0.11	0.09	1.E-01	20	13580	42.84	0.0077	N	N	N/A	N/A	9.18
UNZ-4-5	0.10	0.08	1.E-01	20	15160	47.67	0.0069	N	N	N/A	N/A	11.05
UNZ-4-8	0.11	0.09	1.E-01	20	14200	44.69	0.0066	N	N	N/A	N/A	11.20
UNZ-4-9	0.10	0.09	1.E-01	20	12580	39.67	0.0070	N	N	N/A	N/A	9.24
UNZ-7-19	0.31	0.36	1.E-01	20	4492	14.16	0.0092	N	N	N/A	N/A	2.32
UNZ-7-20	0.33	0.32	1.E-01	20	4442	14.03	0.0107	N	N	N/A	N/A	1.82
UNZ-7-4	0.30	0.29	1.E-01	20	3546	11.18	0.0073	N	N	N/A	N/A	2.49
UNZ-7-5	0.32	0.31	1.E-01	20	3300	10.43	0.0077	N	N	N/A	N/A	2.27
UNZ-7-8	0.31	0.31	1.E-01	20	3858	12.15	0.0077	N	N	N/A	N/A	2.38
UNZ-7-9	0.27	0.26	1.E-01	20	5802	18.29	0.0074	N	N	N/A	N/A	3.85
UNZ-8-4	0.15	0.12	1.E-01	20	11600	36.56	0.0058	N	N	N/A	N/A	11.12
UNZ-8-5	0.19	0.16	1.E-01	20	11540	36.42	0.0053	N	N	N/A	N/A	11.71
UNZ-8-8	0.16	0.13	1.E-01	20	9125	28.79	0.0053	N	N	N/A	N/A	9.39
UNZ-8-9	0.15	0.12	1.E-01	20	12910	40.71	0.0056	N	N	N/A	N/A	12.47
UNZ-2-2	0.13	0.10	1.E-01	20	23562	74.18	0.0055	N	N	N/A	N/A	22.79
UNZ-2-3	0.12	0.10	1.E-01	20	22309	70.24	0.0069	N	N	N/A	N/A	19.83
UNZ-12-2	0.10	0.10	1.E-01	20	29086	91.30	0.0083	N	Y	N/A	N/A	15.15
UNZ-12-5	0.10	0.10	1.E-01	20	27638	86.58	0.0101	N	Y	N/A	N/A	11.36
UNZ-11-1	0.30	0.29	1.E-01	20	8840	27.80	0.0077	N	Y	N/A	N/A	6.35
UNZ-11-5	0.30	0.29	1.E-01	20	7780	24.47	0.0065	N	Y	N/A	N/A	6.25
UNZ-5-15	0.21	0.17	1.E-01	20	13805	43.81	0.0081	N	N	N/A	N/A	11.58
UNZ-1-10	0.20	0.18	1.E-05	900	643	2.02	N/A	N	N	1.40E+11	5.17E-07	N/A
UNZ-1-9	0.20	0.17	1.E-05	900	975	3.08	N/A	N	N	8.98E+10	1.20E-06	N/A
UNZ-4-16	0.12	0.11	1.E-05	900	2041	6.41	N/A	N	N	2.87E+11	5.22E-06	N/A
UNZ-4-17	0.12	0.11	1.E-05	900	2077	6.56	N/A	N	N	2.86E+11	5.46E-06	N/A
UNZ-5-10	0.22	0.20	1.E-05	900	1294	4.06	N/A	N	N	1.77E+11	2.09E-06	N/A
UNZ-5-9	0.22	0.20	1.E-05	900	1277	4.02	N/A	N	N	1.71E+11	2.05E-06	N/A

UNZ-7-15	0.29	0.28	1.E-05	900	1540	4.87	N/A	N	N	2.06E+11	3.01E-06	N/A
UNZ-7-16	0.28	0.27	1.E-05	900	1475	4.80	N/A	N	N	2.01E+11	2.93E-06	N/A
UNZ-8-16	0.18	0.16	1.E-05	900	652	2.30	N/A	N	N	9.09E+10	6.70E-07	N/A
UNZ-8-17	0.18	0.16	1.E-05	900	829	2.72	N/A	N	N	1.09E+11	9.40E-07	N/A
UNZ-4-27	0.10	0.09	1.E-04	900	4696	24.28	N/A	N	N	4.55E+10	7.48E-05	N/A
UNZ-7-21	0.27	0.26	1.E-04	900	7117	22.52	0.0851	N	N	8.38E+10	6.43E-05	N/A
UNZ-4-28	0.10	0.08	1.E-04	900	11337	35.73	0.0529	N	N	1.20E+11	1.62E-04	N/A
UNZ-7-22	0.27	0.26	1.E-04	900	8010	25.27	0.0285	N	N	8.62E+10	8.10E-05	N/A
UNZ-8-21	0.17	0.15	1.E-04	900	7012	22.05	N/A	N	N	7.19E+10	6.17E-05	N/A
UNZ-8-22	0.17	0.14	1.E-04	900	7843	24.60	N/A	N	N	3.83E+10	7.68E-05	N/A
UNZ-5-16	0.21	0.19	1.E-04	900	7625	24.08	N/A	N	N	7.17E+10	7.36E-05	N/A
UNZ-1-14	0.20	0.18	1.E-04	900	5278	16.78	N/A	N	N	3.60E+10	3.57E-05	N/A
UNZ-1-7	0.21	0.19	1.E-03	900	11044	34.70	0.0168	N	N	N/A	1.53E-04	3.65
UNZ-1-8	0.22	0.19	1.E-03	900	10637	33.23	0.0258	N	N	N/A	1.40E-04	2.93
UNZ-4-14	0.12	0.10	1.E-03	900	24575	77.60	0.0189	N	N	N/A	7.64E-04	6.32
UNZ-4-15	0.12	0.11	1.E-03	900	21048	66.40	0.0172	N	N	N/A	5.59E-04	5.75
UNZ-5-7	0.21	0.19	1.E-03	900	16503	52.06	0.0155	N	N	N/A	3.44E-04	4.76
UNZ-5-8	0.21	0.09	1.E-03	900	16566	52.21	0.0171	N	N	N/A	3.46E-04	4.53
UNZ-7-13	0.31	0.31	1.E-03	900	7583	23.90	0.0129	N	N	N/A	7.24E-05	2.67
UNZ-7-14	0.31	0.30	1.E-03	900	7187	22.70	0.0090	N	N	N/A	6.54E-05	3.30
UNZ-8-13	0.16	0.13	1.E-03	900	16384	51.63	0.0299	N	N	N/A	3.38E-04	4.19
UNZ-8-14	0.16	0.13	1.E-03	900	16571	52.07	0.0305	N	N	N/A	3.44E-04	4.43
UNZ-8-15	0.17	0.14	1.E-03	900	14382	45.19	0.0310	N	N	N/A	2.59E-04	3.68
UNZ-1-x	0.22	0.21	1.E-06	900	127	0.34	N/A	N	N	1.20E+11	3.47E-07	N/A
UNZ-1-x	0.22	0.21	1.E-05	900	610	1.94	N/A	N	N	7.00E+10	N/A	N/A
UNZ-1-x	0.22	0.21	1.E-04	900	3682	11.72	N/A	N	N	3.85E+10	N/A	N/A
UNZ-1-x	0.22	0.21	1.E-03	900	8383	26.68	0.9180	N	N	N/A	N/A	N/A

1045 **Table 1. Sample properties, measurement data, experimental conditions, mechanical response and resulting properties of each sample.**

	XRF			Microprobe	
	UNZ-4	UNZ-11	UNZ-12	UNZ-4 glass	standard deviation
SiO$_2$	64.07	65.2	65.48	79.20	0.20
TiO$_2$	0.67	0.66	0.61	0.40	0.01
Al$_2$O$_3$	16.34	15.98	16.39	11.13	0.02
Fe$_2$O$_3$	4.84	4.67	4.35	-	-
FeO	-	-	-	0.92	0.01
MnO	0.10	0.10	0.09	0.01	0.01
MgO	2.57	2.37	2.02	0.07	0.02
CaO	5.18	4.55	4.63	0.56	0.02
Na$_2$O	3.61	3.56	3.69	2.83	0.09
K$_2$O	2.31	2.55	2.46	4.87	0.07
P$_2$O$_5$	0.17	0.12	0.15	-	-
LOI	0.14	0.23	0.14	-	-
Total	100	100	100	100	0

Table 2. Normalised chemical composition of bulk rocks obtained by XRF analysis and interstitial glass obtained by EPMA. UNZ-4 was selected as it is representative of fresh lavas tested in this study; in contrast, UNZ-11 and UNZ-12 were deemed to display a certain degree of alteration. Original totals were 99.97, 100.39, 100.09, and 99.95 for UNZ-4, UNZ-12, UNZ-11, UNZ-4 glass, respectively, before normalisation for
1050 **direct comparison. The standard deviation of the UNZ-4 glass was taken from 2 measurements.**

Sample block name	Average total porosity	Standard deviation	Average connected porosity	Standard deviation	Average isolated porosity	Standard deviation	No. samples
UNZ-1	0.21	0.011	0.18	0.012	0.02	0.002	17
UNZ-2	0.13	0.016	0.11	0.018	0.02	0.003	7
UNZ-4	0.12	0.016	0.12	0.021	0.00	0.016	30
UNZ-5	0.21	0.006	0.19	0.009	0.02	0.006	18
UNZ-7	0.30	0.024	0.29	0.025	0.01	0.002	23
UNZ-8	0.16	0.016	0.14	0.016	0.02	0.003	24
UNZ-11	0.30	0.009	0.29	0.011	0.01	0.004	8
UNZ-12	0.10	0.025	0.09	0.026	0.00	0.002	7
UNZ-13	0.32	0.005	0.30	0.004	0.01	0.004	6

Table 3. Average total, connected, and isolated porosities for each sample block used. A larger number of cores were measured to
1055   **calculate the average porosities than those used in strength tests. *Note: values are presented to 2 d.p. but were calculated with 4 d.p.***